



# Evolution of the Thermodynamic Properties of Clusters of Galaxies out to Redshift of 1.8

Vittorio Ghirardini<sup>1</sup>, Esra Bulbul<sup>1</sup>, Ralph Kraft<sup>1</sup>, Matt Bayliss<sup>2</sup>, Bradford Benson<sup>3,4,5</sup>, Lindsey Bleem<sup>4,6</sup>, Sebastian Bocquet<sup>4,7,8</sup>, Micheal Calzadilla<sup>9</sup>, Dominique Eckert<sup>10</sup>, William Forman<sup>1</sup>, Juan David Remolina Da González<sup>11</sup>, Gourav Khullar<sup>4,12</sup>, Guillaume Mahler<sup>11</sup>, and Michael McDonald<sup>9</sup>

<sup>1</sup>Center for Astrophysics | Harvard & Smithsonian, 60 Garden Street, MA 02138, USA; [vittorio.ghirardini@cfa.harvard.edu](mailto:vittorio.ghirardini@cfa.harvard.edu)

<sup>2</sup>Department of Physics, University of Cincinnati, Cincinnati, OH 45221, USA

<sup>3</sup>Fermi National Accelerator Laboratory, P.O. Box 500, Batavia, IL 60510, USA

<sup>4</sup>Kavli Institute for Cosmological Physics, University of Chicago, 5640 South Ellis Avenue, Chicago, IL 60637, USA

<sup>5</sup>Department of Astronomy and Astrophysics, University of Chicago, 5640 South Ellis Avenue, Chicago, IL 60637, USA

<sup>6</sup>High Energy Physics Division, Argonne National Laboratory, 9700 South Cass Avenue, Lemont, IL 60439, USA

<sup>7</sup>Faculty of Physics, Ludwig-Maximilians-Universität, Scheinerstr. 1, D-81679 Munich, Germany

<sup>8</sup>HEP Division, Argonne National Laboratory, Argonne, IL 60439, USA

<sup>9</sup>Kavli Institute for Astrophysics and Space Research, Massachusetts Institute of Technology, 77 Massachusetts Avenue, Cambridge, MA 02139, USA

<sup>10</sup>Department of Astronomy, University of Geneva, ch. d'Ecogia 16, 1290 Versoix, Switzerland

<sup>11</sup>Department of Astronomy, University of Michigan, 1085 S. University Ave, Ann Arbor, MI 48109, USA

<sup>12</sup>Department of Astronomy and Astrophysics, University of Chicago, Chicago, IL 60637, USA

Received 2020 April 2; revised 2020 October 4; accepted 2020 October 21; published 2021 March 22

## Abstract

The thermodynamic properties of the hot plasma in galaxy clusters retain information on the processes leading to the formation and evolution of the gas in their deep, dark matter potential wells. These processes are dictated not only by gravity but also by gas physics, e.g., active galactic nucleus feedback and turbulence. In this work, we study the thermodynamic properties, e.g., density, temperature, pressure, and entropy, of the most massive and the most distant (seven clusters at  $z > 1.2$ ) clusters selected by the South Pole Telescope and compare them with those of the nearby clusters (13 clusters at  $z < 0.1$ ) to constrain their evolution as a function of time and radius. We find that thermodynamic properties in the outskirts of high-redshift clusters are remarkably similar to the low-redshift clusters, and their evolution follows the prediction of the self-similar model. Their intrinsic scatter is larger, indicating that the physical properties that lead to the formation and virialization of cluster outskirts show evolving variance. On the other hand, thermodynamic properties in the cluster cores deviate significantly from self-similarity, indicating that the processes that regulate the core are already in place in these very high redshift clusters. This result is supported by the unevolving physical scatter of all thermodynamic quantities in cluster cores.

*Unified Astronomy Thesaurus concepts:* Galaxy clusters (584); Intracluster medium (858); Galactic and extragalactic astronomy (563); High-redshift galaxy clusters (2007)

## 1. Introduction

Clusters of galaxies are the largest gravitationally bound objects in the universe and are ideal laboratories to study how cosmic structures form and evolve in time. While the majority of their mass is in the form of dark matter, the hot fully ionized plasma, i.e., the intracluster medium (ICM), retains most of the baryonic component, with only a small contribution from stars and cold gas (3%–5%; Gonzalez et al. 2013). The ICM is observable in the X-ray band mainly through its emission via thermal bremsstrahlung and radiative recombination processes. X-ray observations of clusters of galaxies provide in-depth information about the ICM's thermodynamic properties. The thermal Sunyaev–Zeldovich (SZ) effect, a spectral distortion of the cosmic microwave background caused by the ICM, provides a complementary tool for finding clusters at all redshifts and examining their properties.

X-ray studies of clusters of galaxies provided constraints on thermodynamic properties of the ICM in nearby clusters with redshifts of  $< 0.3$  (e.g., De Grandi & Molendi 2002; Croston et al. 2006; Vikhlinin et al. 2006; Cavagnolo et al. 2009; Arnaud et al. 2010; Pratt et al. 2010; Bulbul et al. 2012). X-ray observations have also provided the serendipitous detection of single high-redshift clusters ( $z > 1$ ; Fabian et al. 2003; Tozzi et al. 2015; Brodwin et al. 2016); however, these studies are

prone to X-ray selection biases (e.g., the cool-core bias; Eckert et al. 2011). The majority of theoretical studies in the literature also focus on predicting thermodynamic properties of the ICM in nearby clusters (Kravtsov & Borgani 2012). In recent years, owing to the wide-area sky surveys performed with the current SZ telescopes, e.g., the South Pole Telescope (SPT; Carlstrom et al. 2011), the Atacama Cosmology Telescope (Fowler et al. 2007), and the Planck mission (Planck Collaboration et al. 2016), it has become possible to detect clusters out to much higher redshifts ( $z \sim 1.8$ ) with a simpler selection function, i.e., the SZ signal tightly correlates with mass (Planck Collaboration et al. 2014; Bocquet et al. 2019). Therefore, X-ray follow-up observations of the SZ-selected clusters provide a unique opportunity to study the evolution of ICM properties in a uniform way.

Integrated X-ray properties of the SPT-selected clusters spanning a large redshift range have been studied in the literature (McDonald et al. 2014; Sanders et al. 2018; Bulbul et al. 2019). Bartalucci et al. (2017a, 2017b) examined the individual thermodynamic properties of the ICM by combining the Chandra and XMM-Newton follow-up observations of a handful of high-redshift clusters ( $z \sim 1$ ) detected by SPT and ACT. Studies of the evolution of the ICM properties in large SZ-selected cluster samples have become possible with large targeted X-ray follow-up programs, e.g., Chandra Large Program (LP). McDonald et al. (2013, 2014)

**Table 1**

Properties of the Sample: Cluster Name, Redshift, Coordinates of the Centroid, Chandra Clean Exposure Time, and XMM-Newton (EPIC MOS1, MOS2, and pn) Clean Exposure Times

Cluster	Redshift	R.A. (deg)	Decl. (deg)	$t_{\text{CXO}}$ (ks)	$t_{\text{MOS1}}$ (ks)	$t_{\text{MOS2}}$ (ks)	$t_{\text{pn}}$ (ks)
SPT-CLJ0205-5829	1.322	31.4437	−58.4855	57.8	69.4	70.2	52.7
SPT-CLJ0313-5334	1.474	48.4809	−53.5781	113.6	186.0	195.2	164.5
SPT-CLJ0459-4947	1.70	74.9269	−49.7872	136.2	461.9	471.6	410.3
SPT-CLJ0607-4448	1.401	91.8984	−44.8033	111.1	132.7	144.8	98.7
SPT-CLJ0640-5113	1.316	100.0645	−51.2204	173.4	127.7	131.9	114.0
SPT-CLJ2040-4451	1.478	310.2468	−44.8599	96.7	76.2	76.6	72.8
SPT-CLJ2341-5724	1.259	355.3568	−57.4158	112.4	107.7	107.7	93.0

studied the stacked thermodynamic properties of SPT-selected clusters in a large redshift range, from 0.3 to 1.2, and in particular reported that the evolution in the electron number density is consistent with the self-similar expectation, where only gravitational forces dominate the formation and evolution of the ICM in the intermediate regions ( $0.15R_{500}-R_{500}$ )<sup>13</sup> of the SPT-selected clusters of galaxies in the redshift range of  $0.2 < z < 1.2$ . The authors also found a clear deviation from self-similarity in the evolution of the core density of these clusters. Deeper Chandra observations of eight high-redshift SPT-selected clusters beyond a redshift of 1.2 confirm earlier results of no evolution in the cluster cores, indicating that active galactic nucleus (AGN) feedback is tightly regulated since this early epoch and self-similar evolution are followed in intermediate regions (McDonald et al. 2017, hereafter MD17). Recently, Sanders et al. (2018) reported a self-similar evolution of the thermodynamic properties at all radii for the same large sample but using a different center and a slightly different analysis scheme out to  $R_{500}$ .

In this work, we combine deep Chandra and XMM-Newton observations of a sample of the seven highest-redshift and most massive SPT-selected galaxy clusters beyond a redshift of 1.2 to study the thermodynamic properties of the ICM and their evolution. We take advantage of the sharp point-spread function (PSF) of Chandra to study the small scales (at this redshift, beyond 1.2, Chandra resolution of  $0''.5$  corresponds to about 5 kpc), while the large effective area of XMM-Newton provides the required photon statistics to measure densities and temperatures out to large scales. Thus, the combination of Chandra and XMM-Newton allows us to obtain precise and extended density profiles and sufficient photon statistics to measure temperature profiles required to probe the evolution of the ICM properties, e.g., density, temperature, pressure, and entropy, out to the overdensity radius  $R_{500}$ . The paper is organized as follows: in Section 2 we present the sample properties and the analysis of the XMM-Newton and Chandra data of the sample, in Section 3 we provide our results, the systematic uncertainties are discussed in Section 4, and we summarize our conclusions in Section 5.

Throughout the paper we assume a flat  $\Lambda$ CDM cosmology with  $\Omega_m = 0.3$ ,  $\Omega_\Lambda = 0.7$ , and  $H_0 = 70 \text{ km s}^{-1} \text{ Mpc}^{-1}$ . All uncertainties quoted correspond to 68% single-parameter confidence intervals unless otherwise stated.

<sup>13</sup>  $R_{500} = \left( \frac{3M_{500}}{4\pi \times 500 \rho_{\text{crit}}(z)} \right)^{1/3}$  is the overdensity radius within which the mean density is 500 times the critical density of the universe

## 2. Cluster Sample and Data Analysis

### 2.1. Cluster Sample

Our sample consists of seven SPT-selected high-redshift ( $z > 1.2$ ) massive clusters of galaxies with signal-to-noise ratio (S/N) greater than 6 and a total SZ-inferred mass greater than  $3 \times 10^{14} M_\odot$  (Bleem et al. 2015). The deep XMM-Newton observations of these clusters have been performed in AO-16 (PIs E. Bulbul and A. Mantz), and Chandra observations were performed in AO-16 through both the XVP program (PI M. McDonald) and two guest observer (GO) programs (PI G. Garmire, S. Murray). The total Chandra and XMM-Newton clean exposure time used in this work is  $\sim 2$  Ms (see Table 1).

### 2.2. Imaging Analysis

#### 2.2.1. XMM-Newton Imaging Analysis

We follow the data analysis prescription developed by the XMM-Newton Cluster Outskirts Project collaboration (X-COP; Eckert et al. 2017) with their new background modeling method (Ghirardini et al. 2018b). We differ from the X-COP analysis by the fact that we use the mean surface brightness for these high-redshift clusters because it is not really possible to compute the median surface brightness profile as done in X-COP, since the cells that will be produced will be very few and highly correlated. See Section 4.2 for how these issues influence our results. Thanks to the reduction of the systematic uncertainty on the background below 5% through this method, we are able to measure thermodynamic properties of high-redshift clusters out to  $R_{500}$ . We provide the summary of the analysis below. We use the XMM-Newton Science Analysis System (SAS) and Extended Source Analysis Software (ESAS; Snowden et al. 2008), developed to analyze XMM-Newton EPIC observations. In our analysis, we use XMM-SAS v17.0 and CALDB files as of 2019 January (XMM-CCF-REL-362).

Filtered event files are generated using the XMM-SAS tasks `mos-filter` and `pn-filter`. The photon count images are extracted from the filtered event files from three EPIC detectors, MOS1, MOS2, and pn, on board XMM-Newton, in the soft and narrow energy band 0.7–1.2 keV. The choice of this narrow band is to maximize the source-to-background ratio and minimize the systematic uncertainties in the modeling of the EPIC background (Ettori & Molendi 2011). To create the total EPIC images, the count images from the three detectors are summed. Next, we use `eexppmap` to compute exposure maps by also taking the vignetting effect into account. The exposure maps are also summed using the scaling factors of 1:1:3.44 for MOS1:MOS2:pn detectors, i.e., the ratio between

the effective area of MOS and pn in the 0.7–1.2 keV energy band. These scaling factors are computed individually for each observation.

The high-energy particle background images are generated by using the background images extracted from the unexposed corners of the detectors and rescaling them to the field of view (FOV). After the light-curve cleaning, residual soft protons still contaminate the FOV (Salvetti et al. 2017). We measure the soft-proton contamination in the FOV of each observation by calculating the fraction of count rates in the unexposed and exposed portions of the detector in a hard band (7–11.5 keV; Leccardi & Molendi 2008). We then generate the 2D soft-proton image (Ghirardini et al. 2018b, as described in their Appendix A), to model the remaining soft-proton contamination. We construct the total non-X-ray background (NXB) by summing the high-energy particle background and the residual soft-proton images. Thus, we obtain total photon images, exposure maps, and total NXB images for each observation.

To detect and excise point and extended sources in the FOV, we use the XMM-SAS tool *ewavelet* with a selection of scales in the range of 1–32 pixels with an S/N threshold of 5. We remove all the point sources found by the *ewavelet* tool from further analysis. We also run CIAO point-source detection tool *wavdetect* on Chandra images. The sources detected on XMM-Newton and Chandra images are combined to remove missed point sources by *ewavelet*. See Section 2.2.3 for details on the Chandra analysis.

### 2.2.2. Point-Spread Function Correction for XMM-Newton

Due to the relatively large size of the PSF of XMM-Newton, some X-ray photons that originate from one particular region on the sky may be detected elsewhere on the detector. XMM-Newton’s 5″-wide PSF (at aim point) needs to be taken into account to correct for this effect due to the small spatial scales of the clusters in our sample (Read et al. 2011). To estimate the impact of the PSF on surface brightness profiles, we first create a matrix,  $\text{PSF}_{ij}$ , whose value is the fraction of photons originating in the  $i$ th annulus in the sky but detected in the  $j$ th annulus on the detector.

In practice, to model the PSF and build the PSF matrix, we, following Eckert et al. (2016, 2020), build an image of an annulus with a constant value inside the annulus itself and zero outside, with the constant chosen in such a way that the sum of all pixels is 1; this represents the probability density function (pdf) for the true photons generated in the annulus that represents their origin on the plane of the sky. The XMM-Newton mirrors smear this annulus-limited pdf onto a larger fraction of the exposed CCDs. We then use a functional form (e.g., a King profile plus a Gaussian as in Read et al. 2011) to model the instrumental PSF function in each location of the detector. The observed photons are the result of the convolution of the original sky photons by the PSF function,  $S_{b,\text{obs}} = \text{PSF} \otimes S_{b,\text{true}}$ . The pdf is no longer limited to the annulus but has spread to the surroundings. The fraction of the pdf, originating from annulus “ $i$ ,” that now is present in annulus “ $j$ ” is the value that we put in the corresponding line and row of the PSF matrix. An example image of the PSF matrix is given in Figure 1. While the majority of the photons that originate from a given annulus are detected in the same region (the largest values are on the diagonal), some fraction of them are detected in a different annulus.

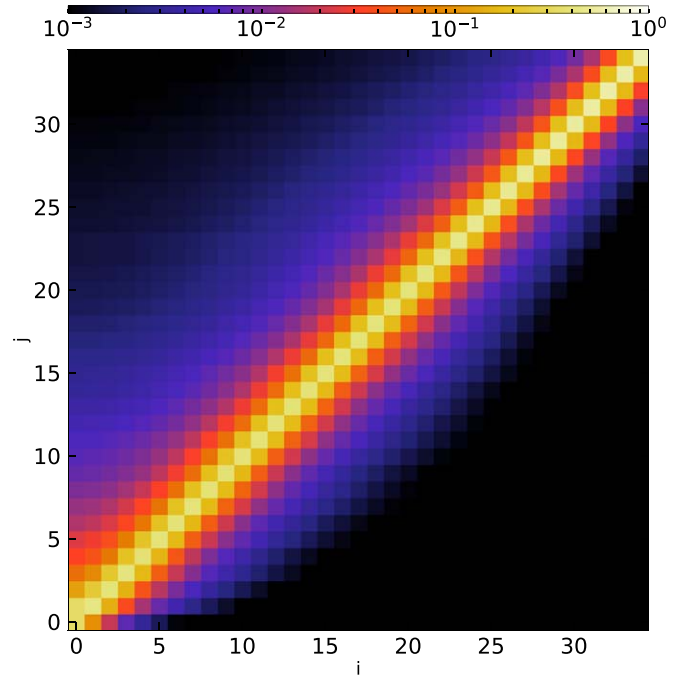


**Figure 1.** Example PSF matrix image used in our analysis. The matrix shows the contribution to the  $j$ th annulus from the  $i$ th annulus at each position  $(i, j)$ . The nondiagonal and asymmetric nature of the distribution shows that the contribution of the emission from the cluster center to the outskirts is not negligible and should be corrected for.

### 2.2.3. Chandra Imaging Analysis

We process the Chandra observations of the sample using the CIAO 4.11 (Chandra Interactive Analysis of Observations; Fruscione et al. 2006) and calibration files in CALDB 4.8.2. We filter the data for good time intervals, including the corrections for charge transfer inefficiency (Grant et al. 2005). We remove the photons detected in bad CCD columns and hot pixels, compute the calibrated photon energies by applying the ACIS gain maps, and correct for their time dependence. We also remove the time intervals that are affected by the background flares by examining the light curves. We ran *wavdetect*, the standard CIAO tool to find point sources in Chandra observations, with scales in the range of 1–32 pixels and a threshold for identifying a pixel as belonging to a source of  $10^{-6}$ . We merge point sources detected on Chandra images with those detected on XMM-Newton images as described in Section 2.2.1. All point sources detected in this process are excluded from further analysis.

We extract photon count images in the soft energy band 0.5–2.0 keV, as is routinely done when analyzing Chandra data.

For the instrumental background we use blank-sky background spectra that are rescaled based on the flux in the hard band 9.5–12 keV to account for variations in the particle background. Exposure maps are generated to correct for the vignetting effect. The particle-background-subtracted, vignetting-corrected images are shown in Figure A1. Due to the small size of Chandra’s PSF, 80% of the total encircled counts are detected within 0″.7 from its source. We therefore do not apply any PSF correction to Chandra data.

### 2.2.4. Joint Chandra and XMM-Newton Surface Brightness Analysis

To compute the surface brightness profile, we first measure the number of photon counts ( $N_{c,i}$ ) in concentric annuli around



**Table 2**  
Best-fit Parameters of the Vikhlinin et al. (2006) Density Model and Measured Background Levels in the Chandra and XMM-Newton Observations

Cluster	$\log(n_0)$	$\log(r_c)$	$\log(r_s)$	$\alpha$	$\beta$	$\epsilon$	$\log(B_{\text{XMM}})$	$\log(B_{\text{Chandra}})$
SPT-CLJ0205-5829	$-4.87 \pm 0.28$	$2.1 \pm 0.4$	$5.6 \pm 0.1$	$1.1 \pm 0.5$	$0.00 \pm 0.04$	$6.2 \pm 0.4$	$-10.99 \pm 0.02$	$-10.81 \pm 0.02$
SPT-CLJ0313-5334	$-4.83 \pm 0.32$	$1.2 \pm 0.8$	$5.6 \pm 0.1$	$1.4 \pm 1.0$	$0.03 \pm 0.03$	$7.0 \pm 0.5$	$-11.07 \pm 0.02$	$-10.48 \pm 0.01$
SPT-CLJ0459-4947	$-3.12 \pm 0.15$	$2.1 \pm 0.2$	$5.3 \pm 0.1$	$1.1 \pm 0.5$	$0.16 \pm 0.03$	$4.7 \pm 0.2$	$-10.78 \pm 0.01$	$-10.09 \pm 0.01$
SPT-CLJ0607-4448	$-3.16 \pm 0.22$	$2.3 \pm 0.3$	$5.2 \pm 0.2$	$1.6 \pm 0.4$	$0.20 \pm 0.05$	$3.2 \pm 0.2$	$-10.53 \pm 0.01$	$-10.18 \pm 0.01$
SPT-CLJ0640-5113	$-3.66 \pm 0.20$	$2.0 \pm 0.4$	$5.1 \pm 0.1$	$1.2 \pm 0.5$	$0.10 \pm 0.03$	$4.3 \pm 0.2$	$-10.78 \pm 0.01$	$-10.38 \pm 0.01$
SPT-CLJ2040-4451	$-5.21 \pm 0.32$	$1.8 \pm 0.5$	$5.7 \pm 0.1$	$0.50 \pm 0.47$	$0.01 \pm 0.04$	$5.5 \pm 0.3$	$-10.39 \pm 0.01$	$-10.45 \pm 0.02$
SPT-CLJ2341-5724	$-3.26 \pm 0.09$	$2.7 \pm 0.1$	$6.0 \pm 0.1$	$0.45 \pm 0.38$	$0.29 \pm 0.01$	$3.2 \pm 0.2$	$-10.48 \pm 0.01$	$-10.61 \pm 0.01$

the cluster center. We find the cluster center by measuring the centroid in a 250–500 kpc aperture on Chandra images following the approach introduced by McDonald et al. (2013). This method allows us to find the center of the large-scale distribution of the intracluster plasma independent of the core morphology. The widths of the annuli are required to be larger than  $2''$ , increasing logarithmically, and with at least 30 counts contained within each annulus. For XMM-Newton the width of these annuli is determined in such a way that each has at least a total of 100 counts and the minimum width is larger than  $5''$ . We then compute the mean exposure time  $t_{\text{exp},i}$  from the exposure map and background counts using the total background map  $N_{\text{NXB},i}$  for the two X-ray telescopes. The surface brightness in each annulus is calculated using the following relation:

$$S_{B,i} = \frac{N_{c,i} - N_{\text{NXB},i}}{t_{\text{exp},i} \cdot A_{\text{reg},i}}, \quad (1)$$

where  $A_{\text{reg},i}$  is the area, in  $\text{arcmin}^2$ , of each annulus “ $i$ .”

From a theoretical point of view, the surface brightness profile is related to the number density through

$$S_{B,i} \propto n_p(r) n_e(r) dl, \quad (2)$$

where  $n_p$  and  $n_e$  are number densities of protons and electrons, respectively, and  $dl$  is the integral along the line of sight. We fit the Vikhlinin et al. (2006) density model to the observed Chandra and XMM-Newton surface brightness data jointly:

$$n_e^2(r) = \frac{n_0^2 \left(\frac{r}{r_c}\right)^{-\alpha}}{\left(1 + \left(\frac{r}{r_c}\right)^2\right)^{3\beta-\alpha/2} \cdot \left(1 + \left(\frac{r}{r_s}\right)^3\right)^{\epsilon/3}}. \quad (3)$$

The parameters of the ICM model are constrained by fitting the observed counts  $N_{c,i}$  in each annulus against the predicted counts  $\mu_i$  (see Equation (5)) using the following Poisson likelihood:

$$-\log \mathcal{L} = \sum_{i=1}^N \mu_i - N_{c,i} \log \mu_i. \quad (4)$$

The net number of counts  $\mu_i$  inferred by the ICM model in the  $i$ th annulus is calculated using the predicted surface brightness, Equation (2), convolved with the PSF matrix, considering the exposed area and time for each annulus, as well as both sky and particle background.

$$\mu_i = \left\{ \sum_j \text{PSF}_{ij} \cdot (S_{b,\text{ICM},i} + B_{\text{sky}}) \right\} \cdot t_{\text{exp},i} \cdot A_{\text{reg},i} + N_{\text{NXB},i}, \quad (5)$$

where  $t_{\text{exp},i}$  and  $A_{\text{reg},i}$  are the exposure time and area of the annulus “ $i$ ,” respectively,  $B_{\text{sky}}$  is the cosmic X-ray background (CXB), and  $N_{\text{NXB},i}$  are the detector background counts.

The sum of XMM-Newton and Chandra likelihoods is used as the total likelihood for the fit. We first minimize the  $\chi^2 = -2 \log \mathcal{L}$  using the Nelder–Mead method (Gao & Han 2012). Then, we fit using the Bayesian nested sampling algorithm MultiNest (Feroz et al. 2009) using shallow Gaussian priors centered around the Nelder–Mead method best-fit results and with a standard deviation of 1 (or 2.3 dex) in order to ensure that the fit is not stuck in a local minimum.

The surface brightness profiles and best-fit models are shown in Figure A2, while the best-fit parameters of the ICM model are given in Table 2. We note that the emissivity measurements of Chandra and XMM-Newton observatories are consistent with each other within 3%; therefore, calibration differences are irrelevant in the measurements of emissivity and number density (as also shown in Bartalucci et al. 2017b).

### 2.3. XMM-Newton Spectral Analysis

We extract spectra using the XMM-ESAS tools `mos-spectra` and `pn-spectra` (Snowden et al. 2008). Redistribution matrices (RMFs) and ancillary response files (ARFs) are created with `rmfgen` and `arfgen`, respectively. The point sources (see Section 2.2.1 for details) are excluded from the spectral analysis. The spectral fitting package XSPEC v12.10 (Arnaud 1996) with ATOMDB v3.0.9 is used in the analysis (Foster et al. 2012). The Galactic column density is allowed to vary within 15% of the measured Leiden/Argentine/Bonn (LAB) Galactic HI survey value in our fits (Kalberla et al. 2005). The extended C-statistics are used as an estimator of the goodness of fit (Cash 1979). The abundances are normalized to the Asplund et al. (2009) solar abundance measurements with the mean molecular weight  $\mu = 0.5994$  and the mean molecular mass per electron  $\mu_e = 1.1548$ , and the ratio of the number density of protons to electrons is equal to  $n_p/n_e = 0.8527$ . The MOS spectra are fitted in the energy band of 0.5–12 keV, while we use the 0.5–14 keV energy band for pn. We ignore the energy ranges between 1.2 and 1.9 keV for MOS, and 1.2–1.7 keV and 7.0–9.2 keV for pn due to the presence of bright and time-variable fluorescence lines. The energy band below 0.5 keV, where the EPIC calibration is uncertain, is eliminated from spectral fits. The source spectrum is modeled with an absorbed single-temperature thermal model `apec` with varying temperature, metallicity, and normalization. For the clusters with multiple observations the model parameters are tied between multiple spectra and fitted jointly.

The particle background is determined using the rescaled filter-wheel-closed spectra, which allows us to measure the intensity and the spectral shape. On top of this, we include an

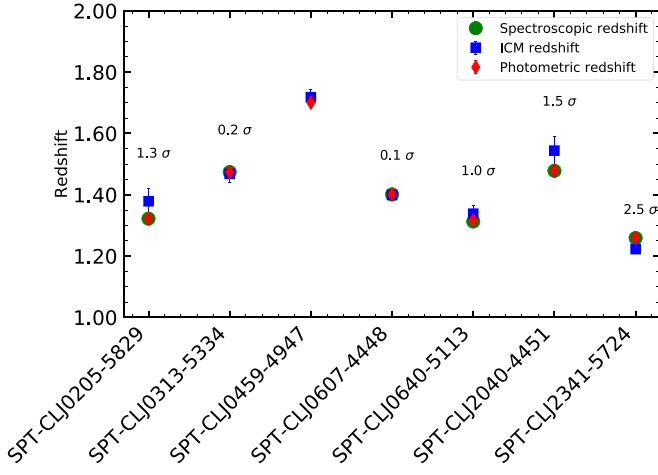


**Figure 2.** Comparisons of X-ray redshifts (in blue) with the photometric redshifts in red (Bleem et al. 2015) and spectroscopic redshifts in green (Bayliss et al. 2014; Stalder et al. 2013; Khullar et al. 2019). The error bars indicate the sum of statistical and systematic uncertainties at the  $1\sigma$  level.

additional model component for the residual soft protons (Salveti et al. 2017), modeled as a broken power law with shape fixed (slopes 0.4 and 0.8 and break energy 5 keV; Leccardi & Molendi 2008) and normalization free. Regarding the sky background, we model it as the sum of three components: (i) the CXB with an absorbed power law with photon index fixed to 1.46, (ii) the galactic halo (GH) with an absorbed APEC model with temperature free to vary in the range of 0.1–0.6 keV, and (iii) the Local Bubble (LB) with an APEC model with temperature fixed to 0.11 keV (Leccardi & Molendi 2008; Snowden et al. 2008). The normalizations of the CXB, LB, and GH background components are set free. To find the sky parameters, we fit the background region, by extracting a spectrum  $5'$  ( $\sim 5R_{500}$ ) away from the core. We impose Gaussian priors on these parameters with width equal to the parameter uncertainty found in the fitting of the background region.

We first extract the XMM-Newton spectra within  $R_{500}$  to measure the redshifts of the clusters from the X-ray data. We fit the spectra within  $R_{500}$ , so that the statistics are of high quality to determine an accurate X-ray redshift. We fit these spectra using an absorbed single-temperature thermal model with free temperature, metallicity, redshift, and normalization. Taking into account the gain calibration uncertainty of XMM-Newton pn at 3 keV (the redshifted position of the Fe–K line) of 12 eV (private communication with the XMM-Newton calibration team), we find that the redshifts are consistent with the previously reported photometric (Bleem et al. 2015) and spectroscopic redshifts (Stalder et al. 2013; Bayliss et al. 2014; Khullar et al. 2019) within the  $2\sigma$  confidence level for these clusters. A comparison of redshifts based on X-ray data with photometric and spectroscopic redshifts is shown in Figure 2. We point out that for SPT-CLJ0459-4947 the previously reported redshift (Bocquet et al. 2019) is measured using the position of the Fe–K line from XMM-Newton data from LP by A. Mantz.

To examine the radial profiles of thermodynamic properties, we next extract the spectra from concentric annuli with sizes increasing logarithmically around the cluster centroid. The minimum width of annuli is set to be  $\sim 15''$  to minimize the effect of XMM-Newton’s PSF, but still having a large enough statistic to determine the projected temperature. We group the

output spectra to ensure having a minimum of 5 counts per bin. The XMM-Newton PSF is taken into account using the cross-talk ARFs generated by the SAS task `arfgen`. This method allows all the spectra to be cofitted by taking into account the cross-talk contribution to an annulus from another region (Snowden et al. 2008; Ettori et al. 2010). The use of flat constant priors on the temperature and metallicity and the use of the “jeffreys” prior on the normalizations (i.e.,  $\text{Prior}(K_{\text{apec}}) = K_{\text{apec}}^{-1}$ ) allow us to account for the uncertainty on the sky background, as well as the uncertainty in their free parameters. The spectra are fit using the Markov Chain Monte Carlo (MCMC) implementation in Xspec of the Goodman-Weare algorithm (Goodman & Weare 2010), with 50,000 steps and 1000 burn-in period to ensure that we investigate the parameter space and derive the uncertainties on free parameters (temperature, metallicity, and normalization) in our fitting software. At the end of this process, we obtain the best-fit projected temperatures and their covariance matrix, which are easily computed using the MCMC chain.

To obtain the 3D deprojected temperature profile of each cluster, we project the ICM temperature model on the plane of the sky by taking into account emission weighting to determine spectroscopic-like temperature (Mazzotta et al. 2004),

$$T_{2D,sl,i} = \frac{\int n_e^2 T_{3D}^{1-\alpha} dV}{\int n_e^2 T_{3D}^{-\alpha} dV}, \quad (6)$$

where  $\alpha = 3/2$ ,  $n_e$  is the electron number density,  $T_{sl}$  is the predicted 2D spectral temperature, and the temperature model  $T_{3D}$  is a widely used phenomenological model to describe the temperature profiles (Vikhlinin et al. 2006).

The 3D ICM model we used in this work is

$$T_{3D}(r) = T_0 \frac{\frac{T_{\min}}{T_0} + \left(\frac{x}{r_{\text{cool}}}\right)^{a_{\text{cool}}}}{1 + \left(\frac{x}{r_{\text{cool}}}\right)^{a_{\text{cool}}}} \frac{1}{\left(1 + \left(\frac{x}{r_i}\right)^2\right)^{\frac{c}{2}}}. \quad (7)$$

We first minimize the  $\chi^2 = -2\log \mathcal{L}$  using the Nelder–Mead method (Gao & Han 2012). Then, the fit is performed with the MCMC method using the code `emcee` (Foreman-Mackey et al. 2013) using Gaussian priors centered around the Nelder–Mead method results and with a sigma of 0.5 (or 1.15 dex). We add an additional prior on the temperature fit, by imposing that the pressure derivative decreases monotonically with radius to maintain convective stability. We use 10,000 steps with burn-in length of 5000 steps to have resulting chains independent of the starting position and thinning of 10 to reduce the correlation between consecutive steps. The likelihood adopted in the fit is

$$\log \mathcal{L} = -(\log T_{\text{obs}} - \log T_{\text{sl}}) \Sigma_{i,j} (\log T_{\text{obs}} - \log T_{\text{sl}})^T, \quad (8)$$

where  $T_{\text{obs}}$  and  $T_{\text{sl}}$  are the arrays of the measured spectral temperatures and of the spectroscopic-like projected temperatures as in Equation (6), respectively, and  $\Sigma_{i,j}$  is the spectral log-temperature covariance matrix (see Section 2.3). Thus, we use a  $\chi^2$ -like log-likelihood, where the temperature distribution in each annulus is assumed to be a lognormal (Andreoni 2012) and the full covariance between the annuli is considered. The best-fit parameters for the temperature profile are given in Table 3. We show an example of the temperature reconstruction process in Figure 3.

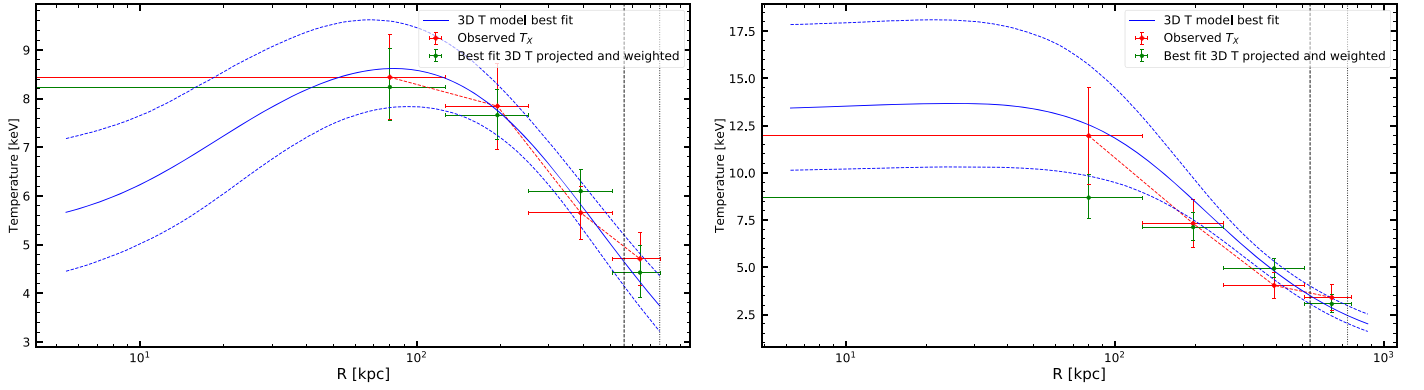


**Figure 3.** Example of the fitting on the temperature profile for SPT-CLJ0459-4947 (left) and SPT-CLJ2040-4451 (right). We show in red the observed 2D temperature profiles, in blue the best-fitting 3D Vikhlinin et al. (2006) temperature profile (with dashed blue lines representing the uncertainties on the reconstructed 3D temperature), and in green the 3D model projected and weighted using the Mazzotta et al. (2004) recipe; thus, green is effectively the best-fitting 2D temperature model.

**Table 3**  
Best-fit Parameters of the Vikhlinin et al. (2006) Temperature Model

Cluster	$T_0$ (keV)	$r_{\text{cool}}$ (kpc)	$r_t$ (kpc)	$\frac{T_{\text{min}}}{T_0}$	$a_{\text{cool}}$	$\frac{c}{2}$
SPT-CLJ0205-5829	$9.5 \pm 2.6$	$14.7 \pm 13.2$	$320 \pm 192$	$0.90 \pm 0.13$	$1.8 \pm 0.6$	$0.36 \pm 0.17$
SPT-CLJ0313-5334	$6.9 \pm 1.5$	$21.4 \pm 15.8$	$348 \pm 185$	$0.77 \pm 0.13$	$1.5 \pm 0.6$	$0.40 \pm 0.18$
SPT-CLJ0459-4947	$9.5 \pm 1.3$	$22.0 \pm 12.8$	$277 \pm 108$	$0.54 \pm 0.16$	$1.8 \pm 0.5$	$0.44 \pm 0.14$
SPT-CLJ0607-4448	$6.0 \pm 0.8$	$24.9 \pm 16.1$	$414 \pm 221$	$0.47 \pm 0.16$	$1.8 \pm 0.5$	$0.29 \pm 0.18$
SPT-CLJ0640-5113	$8.2 \pm 1.4$	$21.4 \pm 14.4$	$299 \pm 133$	$0.60 \pm 0.15$	$1.7 \pm 0.5$	$0.45 \pm 0.16$
SPT-CLJ2040-4451	$14.6 \pm 4.6$	$23.5 \pm 17.8$	$172 \pm 70$	$0.91 \pm 0.12$	$1.7 \pm 0.6$	$0.60 \pm 0.13$
SPT-CLJ2341-5724	$6.5 \pm 1.1$	$25.8 \pm 15.1$	$392 \pm 217$	$0.52 \pm 0.15$	$1.8 \pm 0.5$	$0.29 \pm 0.18$

### 3. Results

In this section we explore thermodynamic properties (e.g., density, temperature, pressure, and entropy) of the high-redshift SPT clusters in our sample taking advantage of the SPT-SZ survey’s clean selection function and its high sensitivity. We further compare the thermodynamic properties of the ICM of the clusters in our sample with the X-COP sample to investigate their evolution with redshift. The X-COP sample is selected based on the Planck S/N including only low-redshift clusters with  $z < 0.1$  (Ghirardini et al. 2018a, hereafter G18). In G18, the authors were able to recover ICM properties out to the virial radius using the joint X-ray and SZ analysis, adding on to the previous studies that probe the region within  $R_{500}$  by joining X-ray and SZ observations (e.g., Ameglio et al. 2007; Bonamente et al. 2012; Hasler et al. 2012; Eckert et al. 2013a, 2013b; Shitanishi et al. 2018). We further remark that the analysis done for the high-redshift clusters is almost identical to the analysis applied in G18 for the X-COP cluster sample, allowing for controlled measurement of the evolution in the thermodynamic quantities. We remark that even though in X-COP three clusters have been excluded from the sample because of disturbed morphology, the X-COP sample is not biased toward relaxed and cool-core clusters: in fact, only 4 of the 12 X-COP clusters can be considered as relaxed; thus, the fraction of cool cores is very similar to what is found in SZ-selected cluster samples (e.g., Rossetti et al. 2017).

The self-similar model (Kaiser 1986), which assumes purely gravitational collapse, predicts a particular evolution with redshift of the cluster properties once they are scaled based on their common quantities, e.g., mass within an overdensity radius (Voit et al. 2005). We therefore measure the mass of our

clusters and rescale our thermodynamic quantities with this mass within  $R_{500}$ . In the next section we describe our method for the mass reconstruction under the assumption of hydrostatic equilibrium (HE) and then show the thermodynamic profiles and describe their properties.

#### 3.1. Total Cluster Mass Reconstruction

A common way to measure the total mass  $M_{500}$  is to use mass proxies calibrated with an X-ray or SZ observable, e.g.,  $L-M$  or  $\xi-M$  scaling relations (e.g., Pratt et al. 2009; Bocquet et al. 2019; Bulbul et al. 2019). However, to avoid introducing a bias into our results by using the evolution in a specific scaling relation, we directly measure the cluster total mass using X-ray observations. The direct measurements based on X-ray data can be obtained from the thermodynamic properties using the assumption of HE and spherical symmetry, i.e.,

$$M(<R) = -\frac{R k_B T}{G \mu m_p} \left[ \frac{d \log \rho_g}{d \log R} + \frac{d \log T}{d \log R} \right], \quad (9)$$

where  $G$  is the gravitational constant,  $m_p$  is the mass of the proton, and  $\rho_g$  is the gas density. There are several methods that are used in the literature to solve the previous equation (see Etti et al. 2013, for a review). Throughout this work, we adopt a “forward” modeling approach to obtain a measurement of  $M_{500}$ , the total cluster mass within  $R_{500}$ . We make use of the best-fitting density and temperature profiles as recovered in Sections 2.2 and 2.3, respectively, propagating them through the HE equation to recover the mass profile. We point out that we forced the pressure profile to be decreasing at all radii.

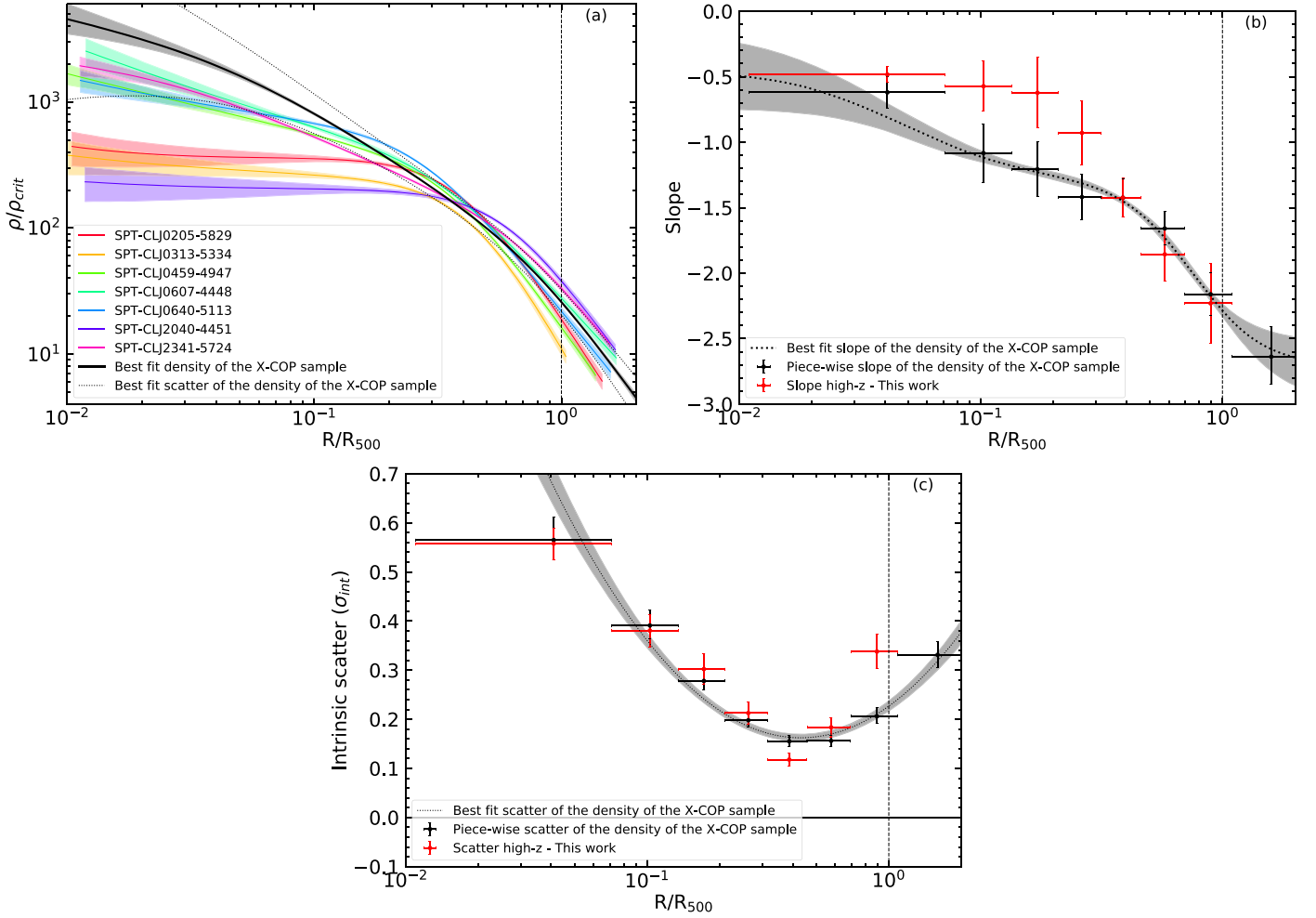


**Figure 4.** (a) Density profiles from the sample. The solid black line represents the average density profile of the X-COP clusters. (b) Slope of the density profile of the high- $z$  SPT-selected clusters obtained by the piecewise power-law fitting technique (shown with red crosses), compared to those of the X-COP clusters (shown with the dotted black line and the black crosses). (c) Scatter in the density profiles of the high- $z$  SPT-selected clusters (red crosses) and the X-COP clusters (black crosses). The vertical dashed line represents the location of  $R_{500}$  in all panels.

This method has the advantage of starting from smooth thermodynamic profiles, where the large number of parameters in these functional forms allows us to reproduce the density and temperature profiles over a large radial range. We direct the reader to the [Appendix](#) for comparison with literature results and with other mass reconstruction techniques we have employed to solve Equation (9).

### 3.2. Density, Temperature, Pressure, and Entropy Profiles

The deprojected electron density profile  $n_e(r)$  (see Section 2.2.4) obtained from surface brightness analysis is first converted into gas density  $\rho(r) = \mu_e m_p n_e(r)$  and then rescaled by the critical density of the universe  $\rho_c = \frac{3H^2(z)}{8\pi G}$ , where  $H(z) = H_0 E(z)$  and  $E^2(z) = \Omega_\Lambda + \Omega_m(1+z)^3$ . Figure 4(a) shows the gas density profiles of the sample. We notice that, in the outskirts, the profiles of the SPT-selected high- $z$  and Planck-selected nearby X-COP clusters are fully consistent with each other, while in the core the SPT-selected high- $z$  profiles are a factor of a few smaller. In the core, the observed scatter (measured as in Equation (6) in [G18](#)) is an order of magnitude in both the SPT-selected high- $z$  and the Planck-selected nearby X-COP clusters, due to the cool-core/non-cool-core states in both samples, i.e., the effect of this dichotomy mostly dominates the scatter near the core. The scatter becomes

minimal around  $0.4R_{500}$ , at the same location where X-COP clusters reach their minima in the scatter. Toward  $R_{500}$  in the outskirts the scatter increases again in both samples. The increase in the high-redshift sample is faster, reaching the value of about 0.35 at  $R_{500}$ , while the scatter in the X-COP sample remains at 0.2 at the same radius. A comparison of the scatter is seen in Figure 4(c).

To be able to measure the slope of the density profiles, we perform a piecewise power-law fitting technique as described in detail in [G18](#). Comparing our sample with the nearby X-COP clusters, we find that in the core the slope in our sample is flatter compared to the X-COP clusters, while in the outskirts ( $>0.3R_{500}$ ) the mean slopes are consistent with each other (see Figure 4(b)).

Next, we study the temperature profiles of the SPT clusters and compare them with the nearby X-COP clusters. For this comparison, the spectroscopic temperature profiles (see Section 2.3 for details) are scaled by the self-similar  $T_{500}$ , also used in Equation (10) of [G18](#) for the X-COP clusters (Voit et al. 2005):

$$T_{500} = 8.85 \text{ keV} \left( \frac{M_{500}}{h_{70}^{-1} 10^{15} M_\odot} \right)^{2/3} E(z)^{2/3} \left( \frac{\mu}{0.6} \right), \quad (10)$$



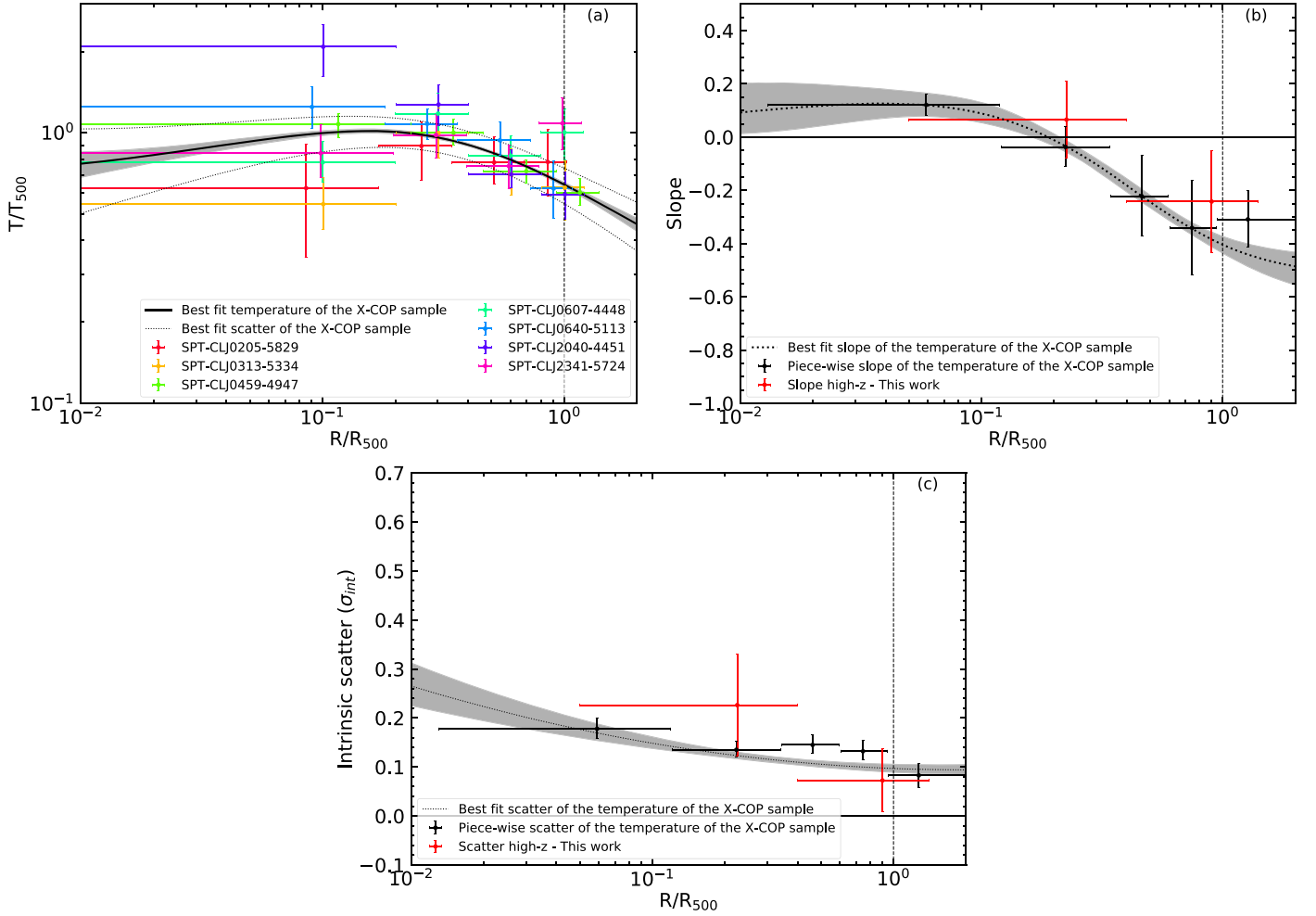


Figure 5. Same as Figure 4, but for the temperature profiles.

where the total mass  $M_{500}$  is measured in Section 3.1 and used self-consistently in calculations of  $R_{500}$  and  $T_{500}$ . In Figure 5(a), we compare the rescaled temperature profiles of the SPT high- $z$  clusters with the nearby X-COP clusters. We find that the scaled temperature profiles in the two samples are consistent with each other in the entire radial range out to  $R_{500}$ . The size of the PSF of XMM-Newton is comparable to the size of the core of these high-redshift clusters; therefore, we cannot resolve well temperatures within  $<150$  kpc, or  $0.1R_{500}$ . Performing a piecewise power-law analysis in two radial bins, we obtain similar slopes and the intrinsic scatter in the temperature profiles when comparing them with the X-COP cluster results.

The pressure profiles are obtained by combining the deprojected density and temperature profiles as  $P = n_e T_e$ . Pressure profiles can be constrained from both X-ray and SZ observations and used for constraining astrophysical properties and the total mass of clusters out to their virial radius (Bonamente et al. 2012; Ghirardini et al. 2018b). We remark that the pressure and entropy profiles within  $0.1R_{500}$  are obtained by combining the resolved density profile with the unresolved temperature profile; hence, results on evolution of pressure profile within this radius depend heavily on the temperature model adopted. The Vikhlinin et al. (2006) temperature model is able to reproduce a variety of cluster

temperature profiles in the core, and the large uncertainty in the inner part of the profile reflects the large width of the central temperature bin. Therefore, in the relevant figures we warn the reader about the possible model-dependent sensitivity of our results using gray shadow areas.

We rescaled the pressure using the self-similar pressure  $P_{500}$  as described in Nagai et al. (2007):

$$P_{500} = 3.426 \times 10^{-3} \text{ keV cm}^{-3} \left( \frac{M_{500}}{h_{70}^{-1} 10^{15} M_{\odot}} \right)^{2/3} E(z)^{8/3} \times \left( \frac{f_b}{0.16} \right) \left( \frac{\mu}{0.6} \right) \left( \frac{\mu_e}{1.14} \right). \quad (11)$$

Figure 6(a) shows a comparison of the rescaled pressure profiles of our sample of high- $z$  clusters with the X-COP sample. We find that in the core of SPT high- $z$  clusters the rescaled pressure is on average lower and flatter compared with what is measured in nearby clusters. In the outskirts, pressure becomes consistent with the finding of low-redshift X-COP clusters. The scatter is also fully consistent between high- and low-redshift clusters in all our radial points except the outermost at  $R_{500}$ , when at high redshift it is 20% higher.

Another thermodynamic property that could be extracted from X-ray observations is the entropy. Entropy is often used to constrain the clumpiness and self-similarity in cluster outskirts (Urban et al. 2011; Walker et al. 2012; Bulbul et al. 2016). The



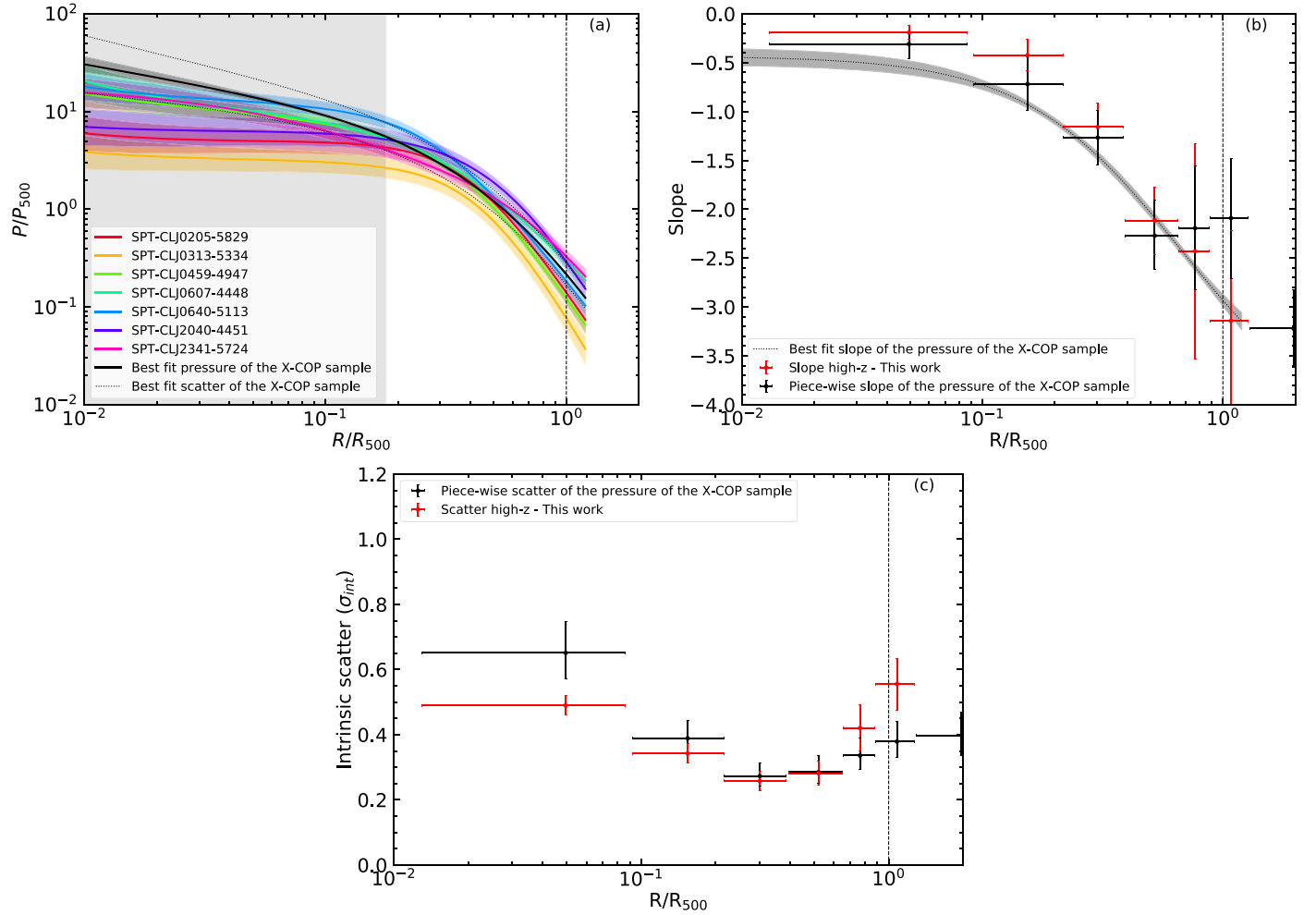


**Figure 6.** Same as Figure 4, but for the pressure profiles. The gray shaded area represents the location within which the temperature profiles are unresolved, where the presented pressure profiles depend on the temperature model adopted.

entropy profiles are obtained using the relation  $K = Tn_e^{-2/3}$ . Similarly, the entropy is rescaled with the self-similar value  $K_{500}$  for comparison (see Voit et al. 2005):

$$K_{500} = 1667 \text{ keV cm}^2 \left( \frac{M_{500}}{h_{70}^{-1} 10^{15} M_{\odot}} \right)^{2/3} E(z)^{-2/3} \times \left( \frac{f_b}{0.16} \right)^{-2/3} \left( \frac{\mu}{0.6} \right) \left( \frac{\mu_e}{1.14} \right)^{2/3}. \quad (12)$$

In Figure 7 we show the entropy profiles of the sample, the slope of the entropy, and the intrinsic scatter. An excess is observed in the entropy compared to self-similarity within  $0.3R_{500}$  near the core. We attribute this excess to nongravitational processes (e.g., AGN feedback, infalling substructures, merging activities) in the cores. A similar entropy excess in the core was reported in nearby low-redshift clusters (Urban et al. 2014; Bulbul et al. 2016; Ghirardini et al. 2018a; Walker et al. 2019), but smaller than the entropy excess observed in these high- $z$  clusters. The high- $z$  entropy excess may be due to the increased incidence of nongravitational effects, e.g., galaxy and cluster formation, and minor mergers at higher redshifts that trigger AGN activity (Hlavacek-Larrondo et al. 2012; McDonald et al. 2016; Bîrzan et al. 2017).

The entropy profiles are flat in the cores and steepen and become consistent with the self-similar model beyond

$\sim 0.2R_{500}$ , similarly to and fully consistent with the entropy profiles in the outskirts of nearby clusters (for a review see Walker et al. 2019, and references therein). The intrinsic scatter is comparable for both samples.

### 3.3. Evolution of Thermodynamic Properties with Redshift

In this section we investigate the redshift evolution of thermodynamic properties of the ICM and measure the deviation from self-similarity of our sample. Following a similar approach described in MD17, we determine the evolution of the density in different radial bins. We characterize the evolution of the thermodynamic quantities using the functions given below:

$$\begin{cases} (\rho)_z = (\rho)_{z=0} \cdot E(z)^{2+C_\rho} \\ (T)_z = (T)_{z=0} \cdot E(z)^{2/3+C_T} \\ (P)_z = (P)_{z=0} \cdot E(z)^{8/3+C_P} \\ (K)_z = (K)_{z=0} \cdot E(z)^{-2/3+C_K} \end{cases}, \quad (13)$$

where  $C_{\rho,T,P,K}$  represent the deviations with respect to self-similar values for the evolution (Kaiser 1986) of density, temperature, pressure, and entropy. Starting from the density, temperature, pressure, and entropy profiles of the nearby X-COP sample, we infer the expected profiles at the redshifts

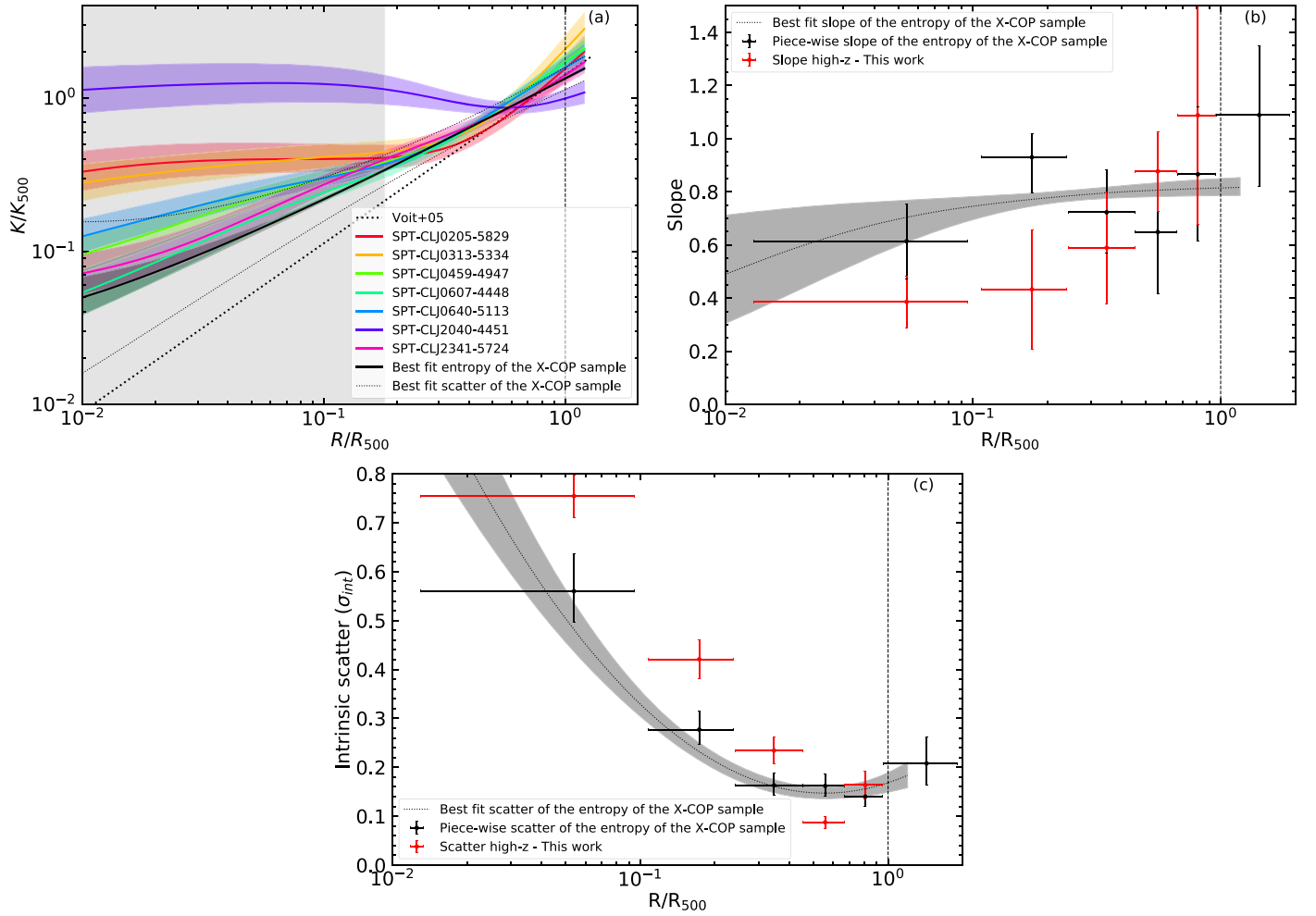


**Figure 7.** Same as Figure 4, but for the entropy profiles. The gray shaded area represents the location within which the temperature profiles are unresolved, where the presented entropy profiles depend on the temperature model adopted.

of the SPT high- $z$  sample assuming a simple deviation from the self-similar evolution, as indicated in Equation (13). We then compare these profiles with the thermodynamic profiles of the SPT clusters using a log-likelihood  $\log \mathcal{L} = -\chi^2/2$  to fit and to determine the best-fit evolution parameters  $C_{\rho,T,P,K}$ . The best-fit parameters of these fits are given in Table 4. The uncertainties of the X-COP profiles, as well as their measured scatter, and the uncertainties on  $R_{500}$  and  $Q_{500}$  (see Equations (10)–(12)) are propagated through the fit. We also include the systematic uncertainties related to our observations in our measurements (see Section 4 for details). The systematic and statistical uncertainties are summed in quadrature to estimate the total uncertainty.

We note that the cluster centers are determined from the Chandra data and initial results are obtained using the centroid of the large-scale ICM emission in this analysis. The choice of cluster center plays an important role especially when measuring the evolution of the central cluster properties (Sanders et al. 2018). To investigate the effect of the center location, we determine the evolution in density using both the centroid and the X-ray peak. The evolution in density, temperature, pressure, and entropy profiles obtained using both the centroids (red) and X-ray peaks (green) is shown in Figure 8.

We find no evolution in the density at small radii ( $\sim 0.3R_{500}$ ) using large-scale centroids. The self-similar evolution in cluster cores is excluded significantly by  $\sim 11\sigma$ . Using the X-ray peaks instead of the centroids, the evolution values move slightly toward self-similarity in the core. However, the departure from self-similarity is still significant at a  $\sim 9\sigma$  confidence level. We also note that the intrinsic scatter in density of high-redshift clusters, shown in Figure 4(c), at small radii is similar to that of the low X-COP redshift clusters. Nongravitational phenomena (e.g., AGN feedback, sloshing) dominate the physical processes in cluster cores and can affect the evolution in the core of the clusters. Thus, our finding may suggest that nongravitational physical processes that regulate cluster cores were already in place since a redshift of 1.8 (with a look-back time of  $\sim 10$  Gyr). Our results in cluster cores are consistent with the results in MD17 at the  $1\sigma$  confidence level. However, the uncertainties in the measurements are reduced at least by a factor of two. Sanders et al. (2018) suggest that use of the X-ray peak instead of centroids could mimic a potential evolution in cluster cores and bias the results in evolution studies. Changing the cluster center does not significantly affect our results.

At large radii, the evolution in density becomes consistent with the self-similar expectation around  $0.1R_{500}$  and remains fully consistent out to  $R_{500}$ . MD17 also reported the best-fit

**Table 4**  
Evolution of the Thermodynamic Quantities with Cosmic Time

(a) Density			
$(R/R_{500})_{\text{in}}$	$(R/R_{500})_{\text{out}}$	$2 + C_\rho$	Sign.
0.01	0.02	$0.01 \pm 0.08 \pm 0.16$	11.2
0.02	0.05	$0.47 \pm 0.06 \pm 0.15$	9.4
0.05	0.08	$0.95 \pm 0.06 \pm 0.15$	6.6
0.08	0.12	$1.32 \pm 0.05 \pm 0.14$	4.5
0.12	0.20	$1.71 \pm 0.04 \pm 0.13$	2.2
0.20	0.30	$1.98 \pm 0.03 \pm 0.12$	0.1
0.30	0.45	$2.07 \pm 0.03 \pm 0.11$	0.7
0.45	0.60	$2.06 \pm 0.04 \pm 0.11$	0.6
0.60	0.80	$2.03 \pm 0.04 \pm 0.12$	0.2
0.80	1.00	$1.98 \pm 0.06 \pm 0.13$	0.1
1.00	1.20	$2.02 \pm 0.07 \pm 0.15$	0.1
(b) Temperature			
$(R/R_{500})_{\text{in}}$	$(R/R_{500})_{\text{out}}$	$2/3 + C_T$	Sign.
0.05	0.20	$0.53 \pm 0.12 \pm 0.17$	0.7
0.20	0.40	$0.78 \pm 0.08 \pm 0.14$	0.7
0.40	0.75	$0.61 \pm 0.09 \pm 0.13$	0.3
0.75	1.40	$0.74 \pm 0.12 \pm 0.12$	0.4
(c) Pressure			
$(R/R_{500})_{\text{in}}$	$(R/R_{500})_{\text{out}}$	$8/3 + C_P$	Sign.
0.01	0.09	$1.86 \pm 0.04 \pm 0.12$	6.1
0.09	0.22	$2.41 \pm 0.05 \pm 0.13$	1.8
0.22	0.39	$2.66 \pm 0.05 \pm 0.15$	0.0
0.39	0.65	$2.71 \pm 0.05 \pm 0.19$	0.2
0.65	0.88	$2.71 \pm 0.07 \pm 0.22$	0.2
0.89	1.28	$2.75 \pm 0.06 \pm 0.25$	0.3
(d) Entropy			
$(R/R_{500})_{\text{in}}$	$(R/R_{500})_{\text{out}}$	$-2/3 + C_K$	Sign.
0.01	0.10	$0.34 \pm 0.06 \pm 0.26$	3.9
0.11	0.24	$-0.27 \pm 0.04 \pm 0.21$	1.8
0.24	0.45	$-0.58 \pm 0.03 \pm 0.17$	0.5
0.45	0.66	$-0.64 \pm 0.03 \pm 0.14$	0.2
0.67	0.95	$-0.57 \pm 0.04 \pm 0.12$	0.8

**Note.** In each single table the first two columns represent the inner and outer radial ranges in which we have looked for the evolution. The third column represents the measured evolution with redshifts, along with its statistical and systematic uncertainty. The fourth column represents the significance measured in number of sigmas of the difference between the measured evolution and the evolution predicted by the self-similar expectation.

evolution consistent with the self-similarity; however, due to the limited statistics, the authors could not rule out no evolution scenario. We tightly constrain self-similarity in cluster outskirts and confirm it with a higher significance level. We also observe an increase of the scatter on cluster density profiles (see Figure 4) in cluster outskirts. This may imply that although the cluster-to-cluster variance in the outskirts increases because of larger mass accretion rates and merger activity at higher redshifts (Wechsler et al. 2002; Fakhouri & Ma 2009; Tillson et al. 2011; Avestruz et al. 2016), the average evolution in density, however, remains consistent with this self-similarity.

In the case of temperature profiles, we do not measure any significant deviation from self-similarity from the cluster cores out to  $R_{500}$ . The intrinsic scatter is also consistent with that of the low-redshift clusters within uncertainties (see Figure 5). Therefore, the cluster temperature evolution and the cluster-to-cluster variance do not seem to change from low to high redshifts. The change of the cluster center makes a very small difference and does not change the results. This is not

surprising considering the large uncertainties on temperature measurements.

We observe a mild evolution in pressure profiles in cluster cores. Similarly, the evolution becomes consistent with self-similarity at  $\sim 0.1R_{500}$  and larger scales. At small scales, pressure profiles deviate significantly from self-similar evolution at a  $6\sigma$  level. Using the X-ray peak as the cluster center does not change the results significantly.

Interestingly, in the core, a mildly significant ( $\sim 3\sigma$  confidence) evolution is observed for the entropy, if we use the centroid as the cluster center. Changing the cluster center to the X-ray peak reduces significantly the observed evolution. In the outskirts the evolution becomes fully consistent with self-similarity, regardless of the center used.

It is important to remind the reader that the evolution measured in cluster cores for pressure and entropy is quite dependent on the adopted cluster temperature model, because the first temperature bin is very large, encapsulating the entire cluster core,  $< 0.1R_{500}$ .

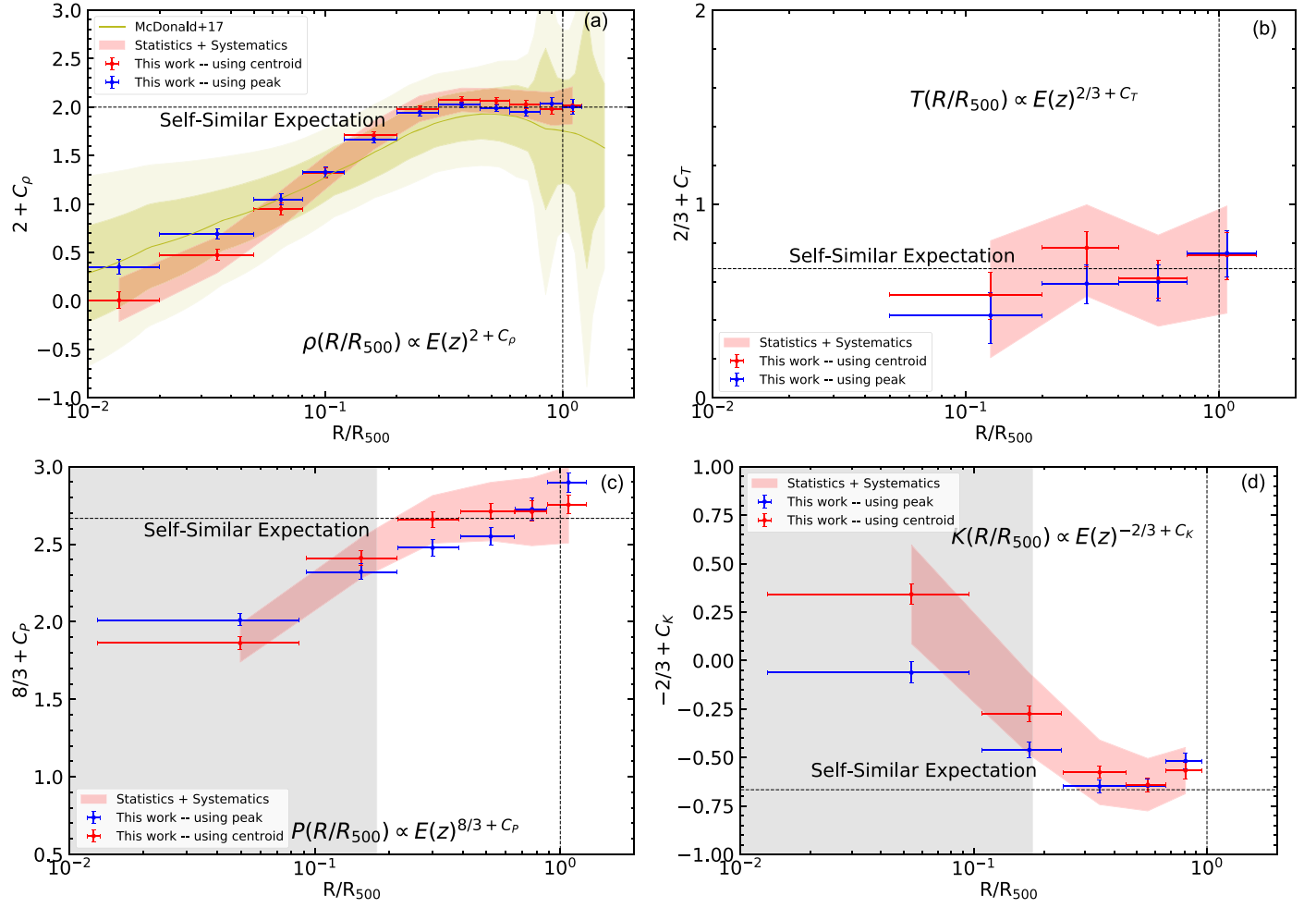


**Figure 8.** (a) Evolution in the density profiles as a function of redshift obtained using the centroid (in red) and X-ray peak (in blue). The red shaded region around our data points represents the sum in quadrature of the statistical and systematic uncertainties (see Section 4 for details). The yellow shaded area represents the same result as found by MD17. Zero values of  $2 + C_\rho$  indicate no evolution with redshift. The self-similar evolution of  $C_\rho = 0$  (corresponding to  $\rho \propto E(z)^2$ ) is represented by a horizontal dashed line. The other panels are the same but for (b) temperature with self-similar predicted evolution corresponding to  $T \propto E(z)^{2/3 + C_T}$ , (c) pressure with self-similar predicted evolution corresponding to  $P \propto E(z)^{8/3 + C_P}$ , and (d) entropy with self-similar predicted evolution corresponding to  $K \propto E(z)^{-2/3 + C_K}$ . Moreover, for pressure and entropy, below  $0.1R_{500}$  the values of the evolution are extrapolated because temperature measurements are not resolved on smaller scales. The vertical dashed line represents the location of  $R_{500}$  in all panels. Moreover, in the panels where entropy and pressure are presented, we mark with gray shaded areas the core region, where the temperature profiles are unresolved.

### 3.4. Polytropic Index

The global structure of the ICM can be effectively described by a polytropic equation of state  $P_e = K\rho^\Gamma$ , where the polytropic index is indicative of stratification of the ICM (Shaw et al. 2010). Both simulations (Komatsu & Seljak 2001; Ostriker et al. 2005; Ascasibar et al. 2006; Capelo et al. 2012) and observations (Markevitch et al. 1998; Sanderson et al. 2003; Bulbul et al. 2010; Eckert et al. 2015; Ghirardini et al. 2019) find that the stratification of the ICM, especially in the outer part, is well represented by a polytropic equation of state with  $\Gamma$  in the range of 1.1–1.3. In particular, the X-COP collaboration reports that the value of  $\Gamma$  in cluster outskirts, where  $\rho/\rho_c \lesssim 400$ , is  $\Gamma = 1.17 \pm 0.01$  at redshifts below 0.1. However, the polytropic index in the high-redshift universe, or its evolution, has never been investigated. We find that the polytropic index (see also Figure 9), is  $1.19 \pm 0.05$  in low-density regions, i.e., in the cluster outskirts. This value is fully consistent with the value measured at low redshifts in the X-COP clusters, indicating that there is no significant evolution with redshift, i.e., the ICM stratification is the same at low and high redshift. In high-density regions, i.e., in the core, we are not able

to resolve the index owing to the large size of the XMM-Newton PSF.

### 4. Systematics

In this section we examine several systematic uncertainties that affect our results on the evolution of the thermodynamic properties of clusters, evaluating their magnitudes. The variation of the thermodynamic property  $Q$  can be converted into the systematic uncertainty on the evolution following the formula below:

$$Q + \Delta Q = E(\hat{z})^k \cdot Q, \quad (14)$$

where  $\hat{z}$  is the average redshift of our sample and  $k$  is the systematic uncertainty on the evolution of each thermodynamic property  $Q$ . Solving this equation for the systematic uncertainty  $k$  gives the following equation:

$$k = \frac{\log\left(1 + \frac{\Delta Q}{Q}\right)}{E(\hat{z})}. \quad (15)$$



**Table 5**  
Range in Which Each Systematic Bias Discussed in Section 4 Affects Each Thermodynamic Quantity in the Core and at  $R_{500}$

Thermodynamic at	HE		Clumping ...	Progenitor		Calibration	
	$0.01R_{500}$	$R_{500}$		$0.01R_{500}$	$R_{500}$	$0.01R_{500}$	$R_{500}$
Density	0.02	0.10	0.058	0.14	0	0.03	0.09
Temperature	0.08	0.10	0.061	0.12	0	0.07	0.04
Pressure	0.10	0.19	0.061	...	...	0.03	0.14
Entropy	0.10	0.11	0.025	0.23	0	0.02	0.01

**Note.** The thermodynamic biases are, from left to right, (1) hydrostatic bias caused by how the profiles are rescaled, (2) clumping bias caused by the presence of unresolved clumps, (3) bias caused by the fact that SPT high- $z$  clusters are not exactly the progenitors of the redshift 0 clusters we are comparing them with, and (4) calibration bias caused by difference between Chandra and XMM-Newton temperatures.

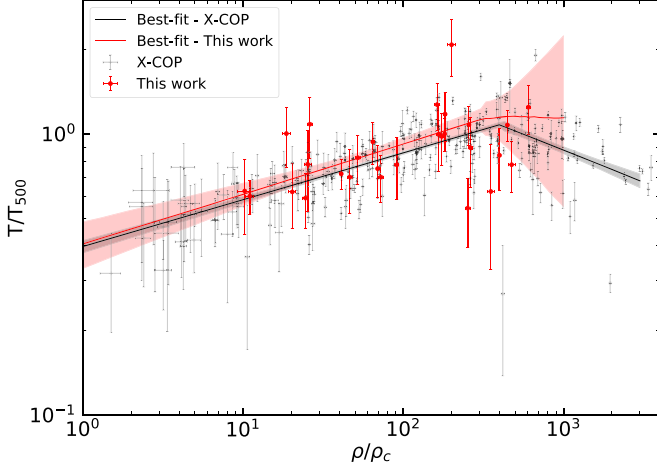


**Figure 9.** Rescaled temperature against rescaled density in high-redshift cluster sample (in red) and in low-redshift clusters (in black; Ghirardini et al. 2019). The lines represent the best-fit broken power law to the data. In particular, we find that the slope in the relation is consistent in low- and high-redshift clusters in the low-density regime, i.e., in cluster outskirts, supporting again the self-similar model of cluster evolution.

We consider the systematic uncertainties related to hydrostatic mass bias, clumping factor, cluster progenitors, and calibration differences between XMM-Newton and Chandra below. In Table 5 we show the amplitude of the mass bias on each thermodynamic quantity in the core and at  $R_{500}$ .

#### 4.1. Mass Bias

The thermodynamic profiles and their evolution depend on the mass that is used to rescale the profiles. However, given that the low-redshift X-COP sample and high-redshift SPT sample have very similar selection criteria, i.e., a selection based on SZ S/N, and the masses are obtained in both cases assuming HE, the mass rescaling is expected to affect the two samples by the same amount; hence, the evolution should not be affected. In this section we search for possible systematics in the hydrostatic mass measurement that affect differently the low- and high-redshift clusters.

An estimate of this mass systematic bias can be obtained by measuring the average ratio between several mass measurements. In Section 3.1 we have described our reference method of solving the HE equation to measure  $M_{500}$ , and in the Appendix we compare this measure with other techniques and other masses in the literature obtained from scaling relations (Bleem et al. 2015; Bocquet et al. 2019). Figure 10 shows the cluster masses obtained through these methods. To estimate the bias, we

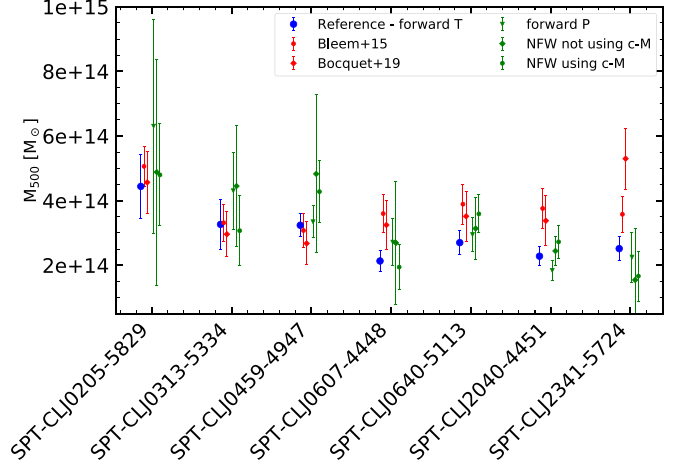


**Figure 10.** Mass comparison for the object in our sample. In red are the masses from the SPT catalog (Bleem et al. 2015) and the masses from the SPT cosmological analysis (Bocquet et al. 2019). In black are the masses recovered by MD17 using the  $M_{\text{gas}}-M_{\text{tot}}$  scaling relation. In green are the NFW best-fit masses in the two cases described in the text. In blue are the forward best-fit  $M_{500}$  computed using a functional form to fit the temperature and density profiles.

calculate the average ratio between the different mass available and the mass obtained using the reference method, described in Section 3.1. Since the error bars are not homogeneous, we apply a bootstrap method, i.e., we measure the mass bias  $10^6$  times, where each time a new distribution of masses is drawn from the masses shown in Figure 10. This method yields a mass bias of  $1 + b = 1.12 \pm 0.01$ . The result implies that high-redshift clusters have potentially 12% higher hydrostatic masses compared to the nearby clusters. Given that clusters at high redshifts are still forming and not yet thermalized, an increase in the nonthermal pressure support due to gas motions in their outskirts and elevated AGN activity in their cores, resulting in an increase in mass bias with redshift, is expected.

If the hydrostatic masses we use in this work are biased (with respect to the low-redshift masses) by a factor of  $(1 + b)$ , this bias translates to a bias in the fiducial radius that can be written as

$$\left(\frac{R}{R_{500}}\right)_z = \left(\frac{R}{R_{500}}\right)_{z=0} \times (1 + b)^{-\frac{1}{3}}. \quad (16)$$

And it translates into an uncertainty on a rescaled thermodynamic property  $Q$  as

$$\left(\frac{Q}{Q_{500}}\right)_z = \left(\frac{Q}{Q_{500}}\right)_{z=0} \times (1 + b)^{-\frac{2}{3}}, \quad (17)$$

where  $Q = T, P, K$ .

Using the mass bias obtained above, we then estimate the corresponding systematic bias in the evolution. This bias affects both  $x$ - and  $y$ -axes, except for density, where the rescaling on the  $y$ -axis is independent of mass. The bias is translated into

$$\Delta Q = \Delta R \cdot \frac{dQ}{dR} = (\Delta M)^{1/3} \cdot \frac{dQ}{dR} \quad (18)$$

on the  $x$ -axis and

$$\Delta Q = (\Delta M)^{2/3} \quad (19)$$

on the  $y$ -axis; then, by summing up in quadrature these two values and applying Equations (14) and (15), we measure the systematic uncertainty on the evolution of the thermodynamic quantities caused by the mass bias.

#### 4.2. Clumping Factor

Unresolved clumps in our observations can lead to higher local densities measured and can bias the observed thermodynamic quantities. In G18 the authors correct the density for the presence of these clumps by both removing the extended sources contaminating the FOV and computing the median of surface brightness distribution in each annulus, which has been shown to be unbiased by the presence of high-density unresolved substructures (Roncarelli et al. 2013; Zhuravleva et al. 2013). In particular, to compute the median, a Voronoi tessellation algorithm needs to be performed (Diehl & Statler 2006) to produce cells containing surface brightness elements. In this work, we eliminate the detected point and extended sources from our analysis. Due to low counts observed and the small extension of the clusters on the sky, the cells produced via the Voronoi tessellation algorithm would be very few and highly correlated with each other. Therefore, it is not possible to compute the median of the surface brightness distribution in the same way as applied to the X-COP sample. Instead, we estimate this bias by adopting the upper limit of 10% within  $R_{500}$  measured in a sample of ROSAT clusters in Eckert et al. (2015). We find that the density profiles are biased by a systematic uncertainty of  $\Delta\rho/\rho = 0.10$ . This translates into a systematic on the density measurements of  $\sim 0.06$  (see Equation (15)).

For the other thermodynamic properties, we combine the effect aforementioned with the bias of 5% in the pressure arising by the presence of clumps (as measured in simulations by Khedekar et al. 2013, where the 5% refers to the upper limit within  $R_{500}$ ). This translates into a bias of 5% on the temperature, consistent with the predicted theoretical bias by Avestruz et al. (2016), and a  $-2\%$  bias on the entropy.

#### 4.3. Progenitors

It is possible that these SPT-selected high-redshift clusters are not the progenitors of the low-redshift clusters in X-COP. In fact, the predicted mass of the SPT clusters is expected to be greater than  $10^{15}M_{\odot}$  at redshift zero when the mass growth curve is taken into account (Fakhouri et al. 2010). Therefore, the SPT-selected clusters are more massive than the X-COP clusters (Ettori et al. 2018), where the reported masses are less than  $10^{15}M_{\odot}$ . We treat the effect due to the fact that the X-COP clusters could be evolved from a different population of clusters than the SPT clusters as a systematic uncertainty.

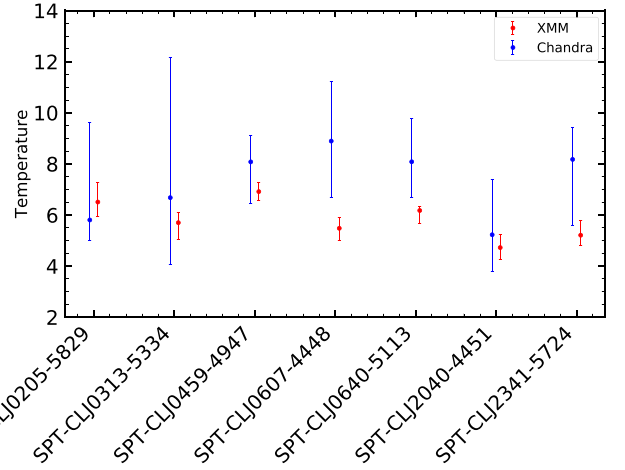


**Figure 11.** Comparison of a single temperature recovered from both Chandra and XMM-Newton from a circular region of width equal in radius to  $R_{500}$ .

To estimate this bias, we assume that the gas density follows the dark matter density as a first approximation. We then use a concentration–mass–redshift relation in Amodeo et al. (2016) to calculate the relative change in the density from a cluster with a mass of  $15 \times 10^{14}M_{\odot}$ , i.e., the expected mass of SPT clusters at a redshift of 0 (Fakhouri et al. 2010), to a mass of  $7 \times 10^{14}M_{\odot}$ , i.e., the average mass of X-COP clusters. Assuming that pressure follows the universal pressure profile, we estimate the thermodynamic quantities. These values are then propagated as systematic errors as shown in Equation (15). The results in the core and in the outskirts are given in Table 5. We note that the self-similar model predicts an evolution that is independent of mass. Therefore, once the thermodynamic quantities are rescaled with their self-similar value, the fact that they are too massive to be the progenitors of the X-COP clusters is of minor importance, especially at large radii.

#### 4.4. Calibration Difference between Chandra and XMM-Newton

Calibration differences between Chandra and XMM-Newton are described in the literature. Temperature measurements can be biased up to 40% depending on the energy band used and cluster temperature (e.g., Schellenberger et al. 2015, and references therein). On the other hand, density measurements by Chandra and XMM-Newton are fully consistent within the uncertainties (see Bartalucci et al. 2017a; see also Section 2.2.4).

To quantify the bias due to calibration differences, we extract both XMM-Newton and Chandra spectra of the region within  $R_{500}$  and fit the spectra using a single-temperature thermal *apex* model. We note that in the case of the SPT high-redshift clusters it is not possible to measure temperature profiles using Chandra observations in several radial bins owing to the limited statistics. A comparison of measured single temperatures is shown in Figure 11. We find that the temperature measurements are consistent with each other within statistical uncertainties. However, we note that the uncertainties on the Chandra measurements are large because of limited statistics.

To estimate the systematic uncertainty on each thermodynamic quantity  $Q$  caused by this discrepancy in the temperature is not trivial. The increase of the temperature would lead to an increase in the total mass by the same amount, if the slope of the temperature profile does not change. Schellenberger et al. (2015) report that temperature measurements based on Chandra data are,

on average, 17% higher than those derived from XMM-Newton for the average mass of the clusters in our SPT sample. Thus, a systematic of 17% on the temperature becomes a 17% systematic on the mass, and thus a 5.7% bias on  $R_{500}$  (one-third considering the propagation of uncertainty) and 11.3% bias on  $Q_{500}$  (two-thirds considering that all self-similar quantities depend on mass with power of  $2/3$ ). Thus, the variation on each thermodynamic quantity is

$$\frac{\Delta Q/Q_{500}}{Q/Q_{500}} = \underbrace{17\%}_{\text{on } Q} - \underbrace{11.3\%}_{\text{on } Q_{500}} - \underbrace{5.7\% \cdot \frac{dQ}{dR}}_{\text{on } R_{500}}. \quad (20)$$

We point out that, for the last two terms, the variation on the rescaled thermodynamic quantity from the radial and the  $Q_{500}$  rescaling is in the opposite direction with respect to the systematic bias on the quantity  $Q$ . Thus, by computing the slope at each radius, we get the relative rescaled thermodynamic variation at each radii, and finally, using Equation (15), we obtain the systematic bias affecting the evolution of each thermodynamic quantity as given in Table 5.

## 5. Conclusions

In this paper we have studied the thermodynamic profiles for the seven most massive clusters at redshift above 1.2 in the SPT-SZ survey. These clusters were observed by both Chandra and XMM-Newton for a total clean exposure time of about 2 Ms. We combine the data from these two telescopes to recover density, temperature, pressure, and entropy profiles and examine their evolution with redshift from cluster cores to outskirts. Furthermore, we measure the temperature profiles of a complete set of SPT-selected high-redshift clusters for the first time, allowing us to reconstruct the total cluster masses under the assumption of HE. Our results include the systematic uncertainties that are extensively studied in Section 4.

Deep XMM-Newton observations of the SPT-selected clusters have sufficient statistics to determine the redshifts from the X-ray data alone. The Fe–K line at 6.7 keV (rest frame) is clearly detected in the spectrum of each cluster in the sample. The centroids of these emission lines are used to measure the redshifts. We show that the redshifts obtained from the X-ray data of the SPT high- $z$  clusters are consistent with the previously reported redshifts obtained through optical photometry and spectroscopy (Bayliss et al. 2014; Bleem et al. 2015; Khullar et al. 2019).

Combination of Chandra’s high spatial resolution and XMM-Newton’s large FOV and effective area is the most powerful way to measure thermodynamic profiles of clusters at high redshifts,  $z > 1.2$  from their cores ( $0.01R_{500}$ ) to the outskirts ( $R_{500}$ ). Accurate measurements of temperature profiles enable a few key measurements for these clusters, e.g., total mass, pressure, and entropy. We are able to measure their total mass through the HE assumption with relatively small uncertainties (10%–20%) at these redshifts. The hydrostatic masses are generally in good agreement with reported masses in the literature obtained through SZ S/N and scaling relations (Bleem et al. 2015).

We further measure the density, temperature, pressure, and entropy profiles of the high- $z$  SPT cluster sample and compare their distributions with the previously reported thermodynamic properties of the nearby X-COP clusters. The scatters of all the thermodynamic quantities are similar in low- and high-redshift

clusters in small spatial scales near the cores. At large radii, the scatter increases more steeply in the sample of high-redshift clusters. This may be due to an increased frequency of merger events and higher mass accretion rate at high redshifts (Wechsler et al. 2002; Fakhouri & Ma 2009; Tillson et al. 2011).

The average profiles of density, temperature, pressure, and entropy of high- $z$  clusters are self-similar and consistent with those of the X-COP clusters at large spatial scales near  $R_{500}$ . Temperature profiles of high-redshift clusters are self-similar at all radii. We also report that the polytropic index ( $1.19 \pm 0.05$ ) is fully consistent with that measured at low-redshift clusters, indicating that there is no significant evolution with redshift. The high observed scatter in density, pressure, and entropy in cluster cores is due to the cool-core/non-cool-core dichotomy in these cluster samples. The scatter in the thermodynamic properties becomes minimal at  $0.4R_{500}$  and increases toward  $R_{500}$  in the SPT-selected high- $z$  clusters. The increase in the merger frequency and mass accretion rate in high- $z$  clusters may contribute to high scatter in cluster outskirts (Wechsler et al. 2002; Fakhouri & Ma 2009; Tillson et al. 2011).

We are also able to constrain the evolution in density and temperature profiles of the cluster. Measurements of the evolution in entropy and pressure profiles with redshift also become available owing to precise temperature constraints for the first time. We find that the evolution in thermodynamic profiles deviates significantly from the self-similar evolution in cluster cores, while in the outskirts the profiles are on average in agreement with the prediction from the self-similar model. We find no evidence for evolution in the density in cluster cores, confirming the results in MD17. We point out that the analysis performed in this paper and the one in MD17 are different in how self-similarity has been probed. We have considered two high-S/N cluster samples at low and high redshift, while in MD17 the authors have considered  $\sim 100$  low-S/N clusters. Therefore, it is striking that two different analyses on two different samples yield the same results on the evolution of cluster density profiles. We observe only mild evolution in pressure and entropy profiles in cluster cores. On the other hand, the evolution of temperature profiles is in agreement with self-similarity. Utilization of the X-ray peak instead of the centroid of the large-scale emission does not significantly affect our results (it changes the measured evolution in the core toward self-similarity but does not change significantly the significance).

Planned and future X-ray telescopes with sufficiently small spatial resolution and large effective area (e.g., Athena, Lynx) will provide sufficient statistics to precisely measure temperature and density profiles down to kiloparsec scales in the cores of a large sample of clusters (Nandra et al. 2013; Gaskin et al. 2019). These measurements will allow us to probe in detail the role of AGN feedback in the first clusters formed and to shed light on the accretion processes in cluster outskirts and the structure formation in the universe.

This work was performed in the context of the South Pole Telescope scientific program. S.P.T. is supported by the National Science Foundation through grant PLR- 1248097. Partial support is also provided by the NSF Physics Frontier Center grant PHY-0114422 to the Kavli Institute of Cosmological Physics at the University of Chicago, the Kavli Foundation, and the Gordon and Betty Moore Foundation grant GBMF 947 to the University of Chicago. This work is also supported by the U.S. Department of Energy. Work at

Argonne National Lab is supported by UChicago Argonne LLC, Operator of Argonne National Laboratory (Argonne). Argonne, a U.S. Department of Energy Office of Science Laboratory, is operated under contract No. DE-AC02-06CH11357. B.B. is supported by the Fermi Research Alliance LLC under contract No. De-AC02-07CH11359 with the U.S. Department of Energy. G.M. received funding from the European Union’s Horizon 2020 research and innovation programme under the Marie Skłodowska-Curie grant agreement No. 896778.

*Facility:* 10 m South Pole Telescope (SPT-SZ)—Chandra X-ray Observatory—XMM-Newton.

## Appendix Mass Reconstruction

In this appendix we solve the HE equation with other approaches besides the one used throughout this paper; see Section 3.1. We also show the particle-background-subtracted, vignetting-corrected images of the clusters in Figure A1, and the Chandra and XMM-Newton measured NXB-subtracted surface brightness profiles and best-fit models in Figure A2.

### A.1. Forward Modeling Approach

In Section 3.1 we have used a “forward” modeling where a temperature model is combined with a density model to solve the HE equation and recover the mass profile. However, it is possible to do the same using a pressure model in combination with the density model, because it would be the equivalent of doing the same but using pressure divided by density as the temperature model. We use the five-parameter functional form (Nagai et al. 2007) to model the pressure and then recover the 3D temperature profile by dividing it by the density profile.

Then, everything goes like in Section 3.1. We indicate this method “forward P.” distinguishing it from the one used in Section 3.1, indicated as “forward T.”

### A.2. Backward Modeling Approach

A popular model used in the literature is the “backward” modeling, which assumes a dark matter distribution, e.g., the Navarro–Frenk–White (NFW) model (Navarro et al. 1997), and then the observed temperature profiles are fitted against their profiles as predicted by the combination of the mass model with the density profile. Only two parameters are required to fully characterize the NFW mass model, scale radius and concentration (see Ettori et al. 2010, for details):

$$M_{\text{tot,NFW}} = \frac{4}{3}\pi\rho_c(z)500\frac{r_s^3c_{500}^3}{\log(1+c_{500}) - \frac{c_{500}}{1+c_{500}}} \times \left( \log\left(1 + \frac{r}{r_s}\right) - \frac{\frac{r}{r_s}}{1 + \frac{r}{r_s}} \right), \quad (\text{A1})$$

or using the equation  $R_{500} = r_s c_{500}$ ,

$$M_{\text{tot,NFW}} = \frac{4}{3}\pi\rho_c(z)500\frac{R_{500}^3}{\log(1+c_{500}) - \frac{c_{500}}{1+c_{500}}} \times \left( \log\left(1 + c_{500}\frac{r}{R_{500}}\right) - \frac{c_{500}\frac{r}{R_{500}}}{1 + c_{500}\frac{r}{R_{500}}} \right). \quad (\text{A2})$$

Since the large bin size of the annuli is caused by the large XMM-Newton PSF of about  $15''$ , which corresponds to a physical size of 150 kpc, the constraints on the concentration parameter are



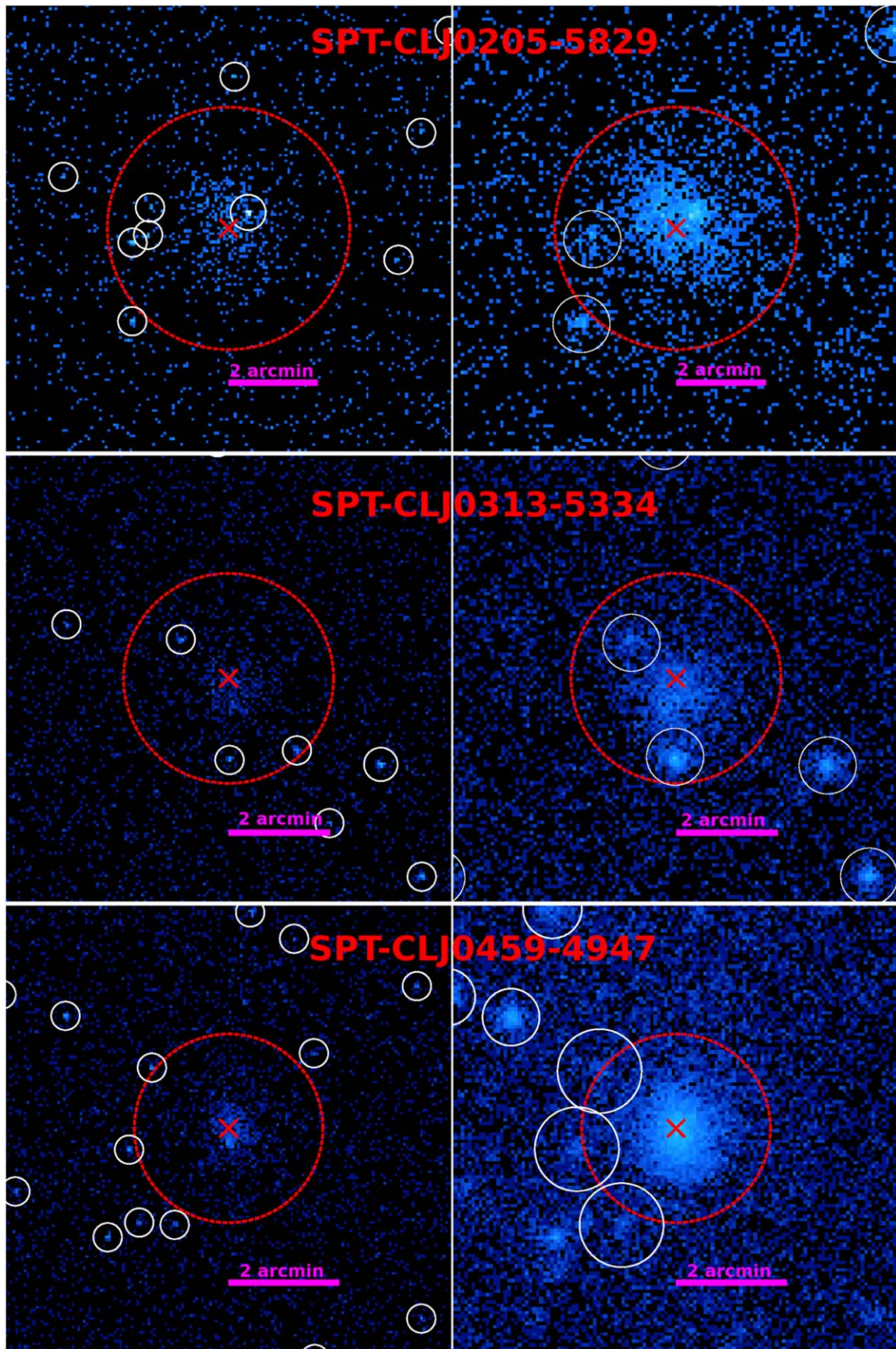


**Figure A1.** Raw count images of the clusters; Chandra counts are shown on the left, while the XMM-Newton image is shown on the right. The blue cross indicates the location of the center used, and the white circles indicate the point sources masked.



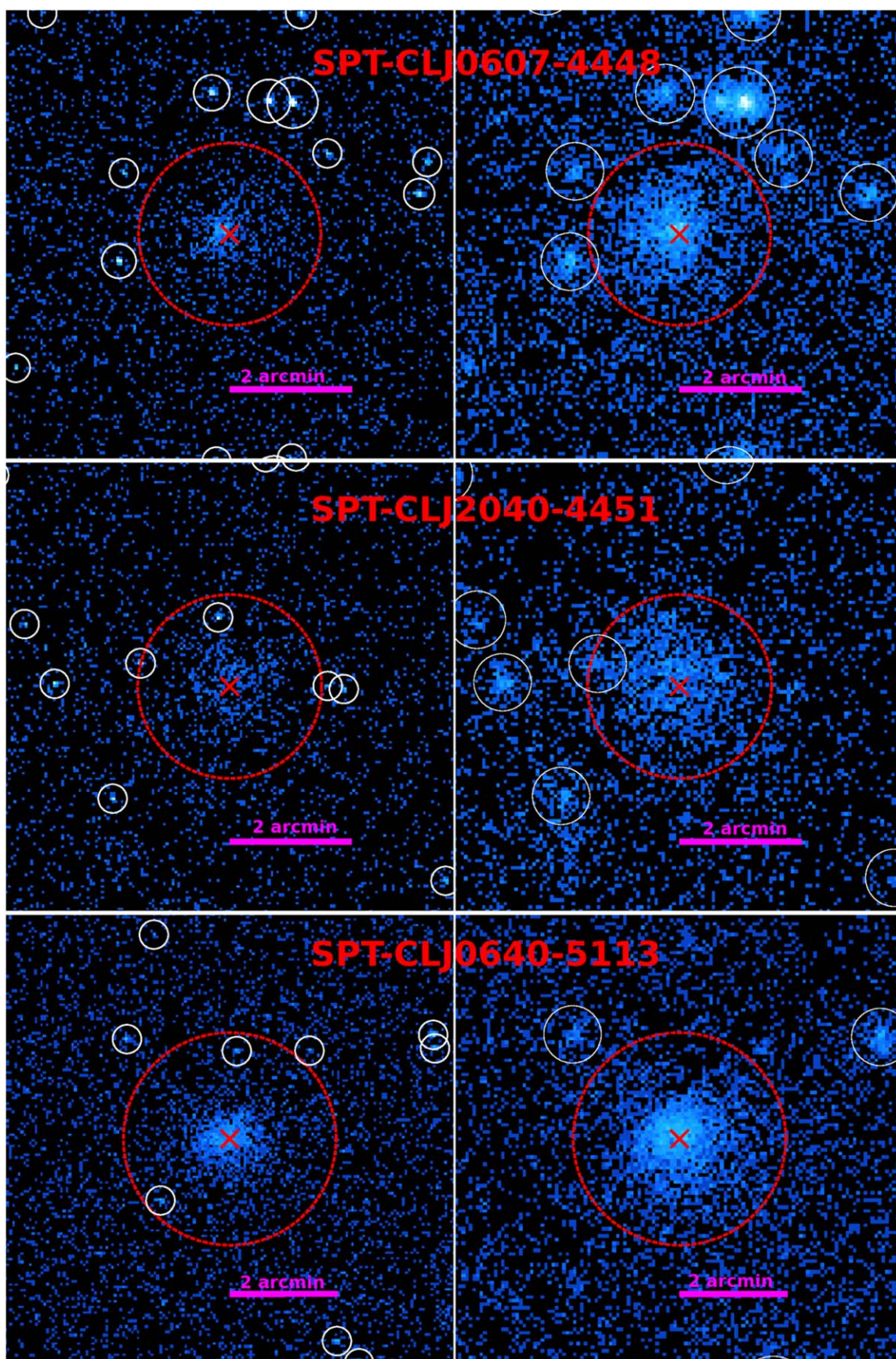


Figure A1. (Continued.)



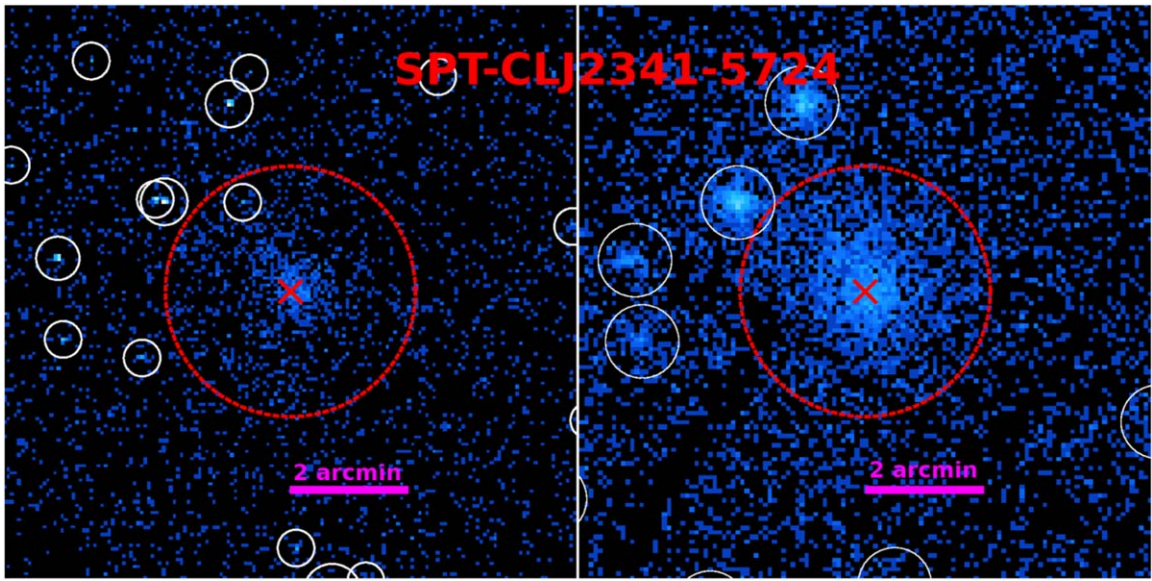


Figure A1. (Continued.)

very weak, meaning that the concentration is almost unconstrained. Thus, we apply this technique two times, once leaving concentration completely free, i.e., with flat priors, and once choosing a Gaussian prior on the concentration parameter, centered on the concentration–mass relation provided by Diemer & Joyce (2018)<sup>14</sup>:  $\log c_{500} = 0.885 - 0.049 \log(M_{500}/5 \times 10^{14} M_{\odot})$ , and with an intrinsic scatter of  $\sigma_{\log_{10}(c_{500})} = 0.1$  (from Neto et al. 2007) propagated through our analysis.

The fit is done using the code `emcee` (Foreman-Mackey et al. 2013), starting from a standard maximum likelihood fit,  $\chi^2$  minimization using the Nelder–Mead method (Gao & Han 2012), using 10,000 steps with burning length of 5000 steps to have resulting chains independent from the starting position, and thinning of 10 in order to reduce the correlation between consecutive steps.

### A.3. Reconstructed Mass

Our reconstructed  $M_{500}$ , using the method described above and in Section 3.1, are shown in Figure 10, and displayed in Table 6. We compare our mass reconstruction among themselves, and with the SPT masses as calculated in the catalog (Bleem et al. 2015) using the  $M$ – $\zeta$  fixed scaling relation, with the masses calculated from the scaling relations obtained

for the SPT cosmological results (Bocquet et al. 2019), and with the masses used in MD17, which come from the  $M_{\text{gas}}$ – $M_{\text{tot}}$  scaling relations (Vikhlinin et al. 2009). Overall the masses we measure are consistent with all the other masses we are comparing with, with two peculiar cases: (1) SPT-CLJ0459-4947, for which the masses coming from the *forward* reconstruction agree with the other masses in the literature, i.e., the two SPT masses and the masses in MD17, but the NFW reconstruction prefers a higher mass. This can potentially indicate that the NFW mass model could not be the best model to describe the dark matter potential for this object. (2) SPT-CLJ2341-5724, which has all the masses coming from our analysis consistent within  $1\sigma$ ; however, when comparing with the literature masses, we find that these are much higher than what we measure, indicating the possibility that this cluster does not fall on the scaling relations used to determine the literature masses. The recovered mass of SPT-CLJ0205-5829 has very large uncertainties. This is because the XMM-Newton 55 ks observation 0803050201 is highly flared, with only about 10 ks remaining after flare removal, and on top of that this cluster has a point source very close to the cluster center, thus decreasing the photon statistics, with the resulting effect being larger error bars for the temperature, translating into large error bars on the mass since  $M \sim T$ .

<sup>14</sup> As implemented in the code `COLOSSUS` (Diemer 2017), with  $\Omega_m = 0.3$ ,  $\Omega_{\Lambda} = 0.7$ ,  $\sigma_8 = 0.8$ ,  $H_0 = 70 \text{ km s}^{-1} \text{ Mpc}^{-1}$ .

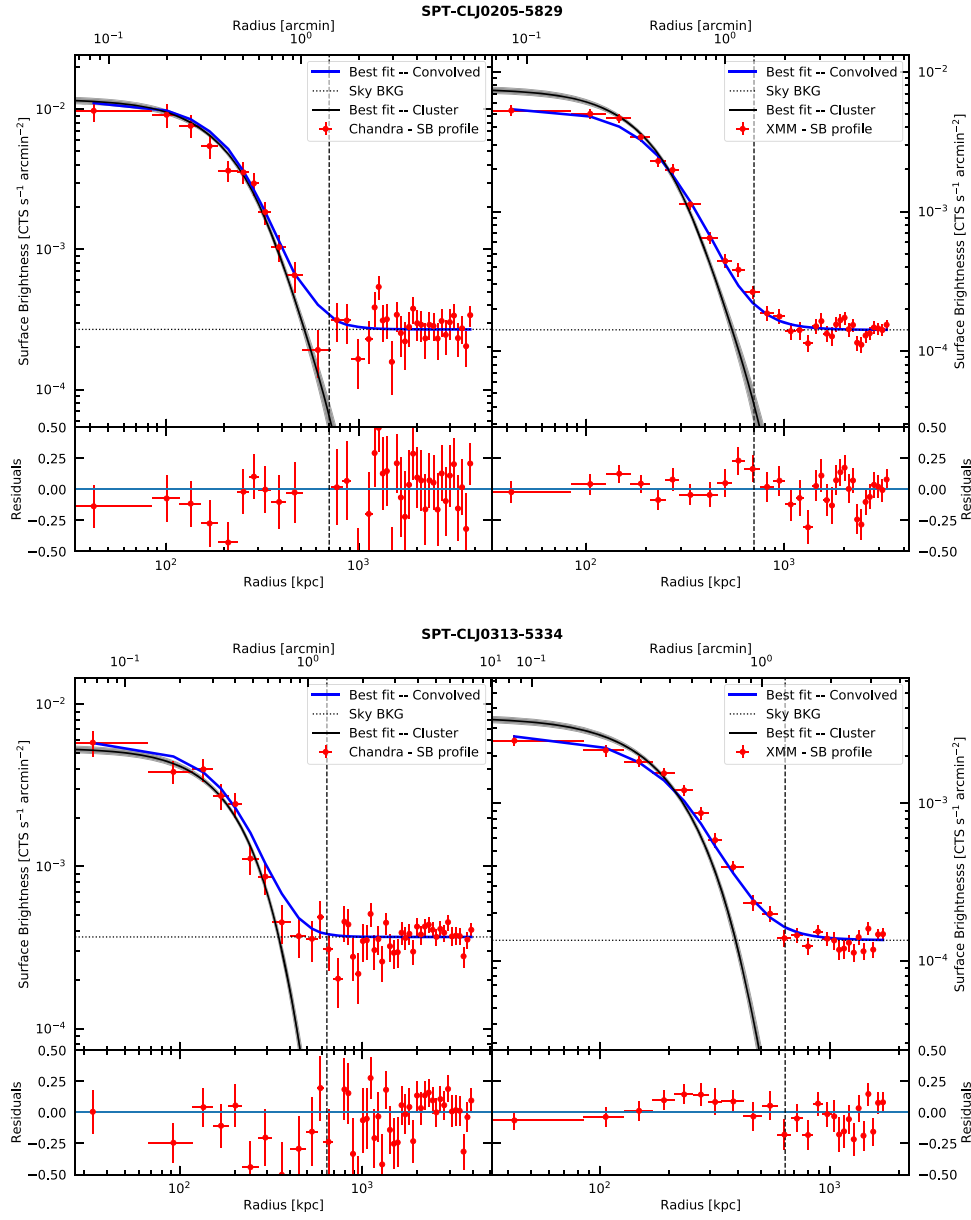


**Figure A2.** Chandra (left) and XMM-Newton (right) measured NXB-subtracted surface brightness (red points). The best-fitting model is the Vikhlinin et al. (2006) functional (solid black line) form plus a constant sky background (horizontal dotted line); it is convolved with the instrumental PSF and is shown with a blue line. In the case of Chandra the PSF is simply a diagonal matrix with ones on the diagonal, while for XMM-Newton it is calculated as in Section 2.2.2. In the bottom panels we show the residuals ( $\frac{\mu_i - N_{c,i}}{N_{c,i}}$ ). The dashed vertical line represents the location of  $R_{500}$ , as measured by solving the HE equation (Equation (9)) using the “forward T” method (see Section 3.1).



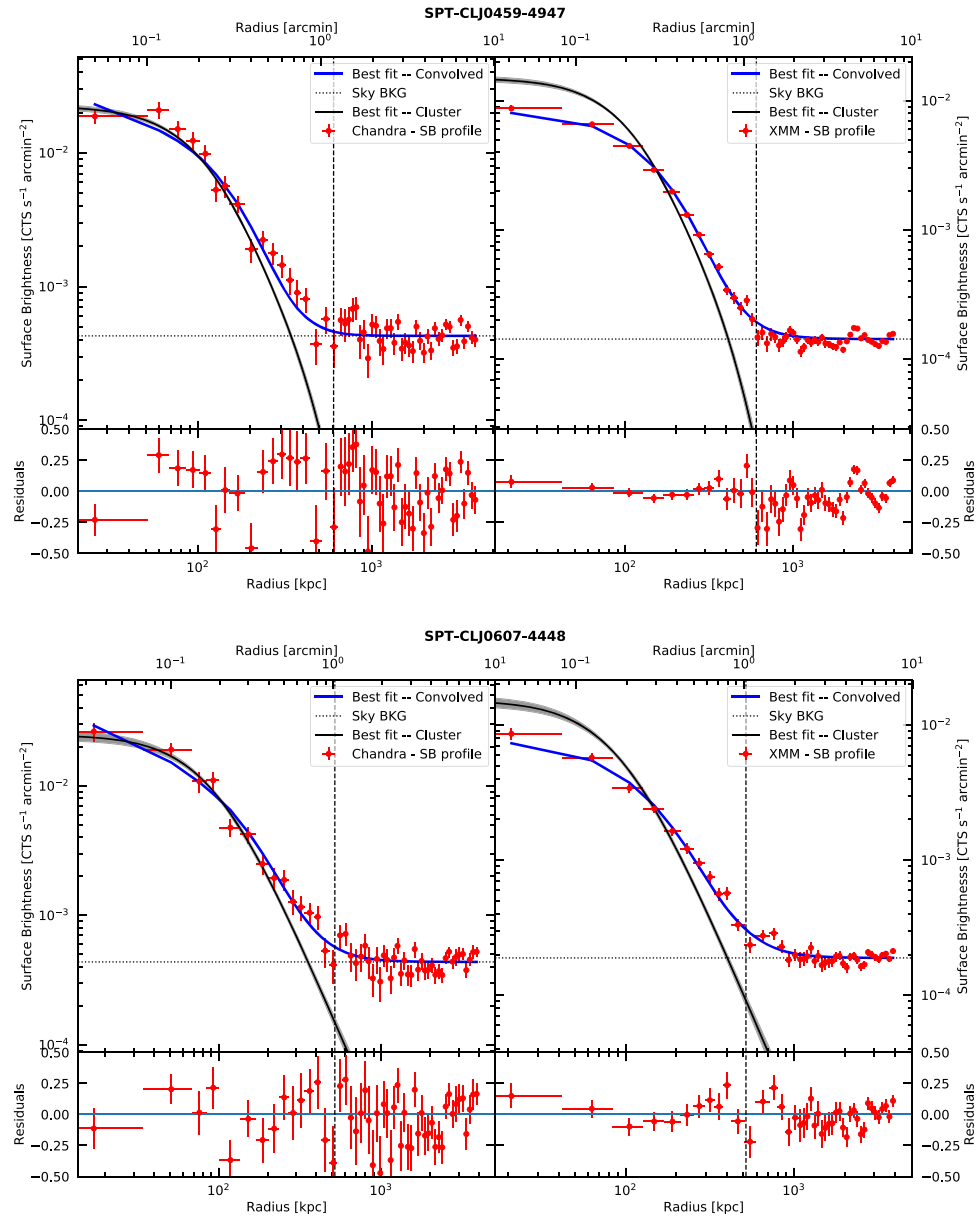


Figure A2. (Continued.)

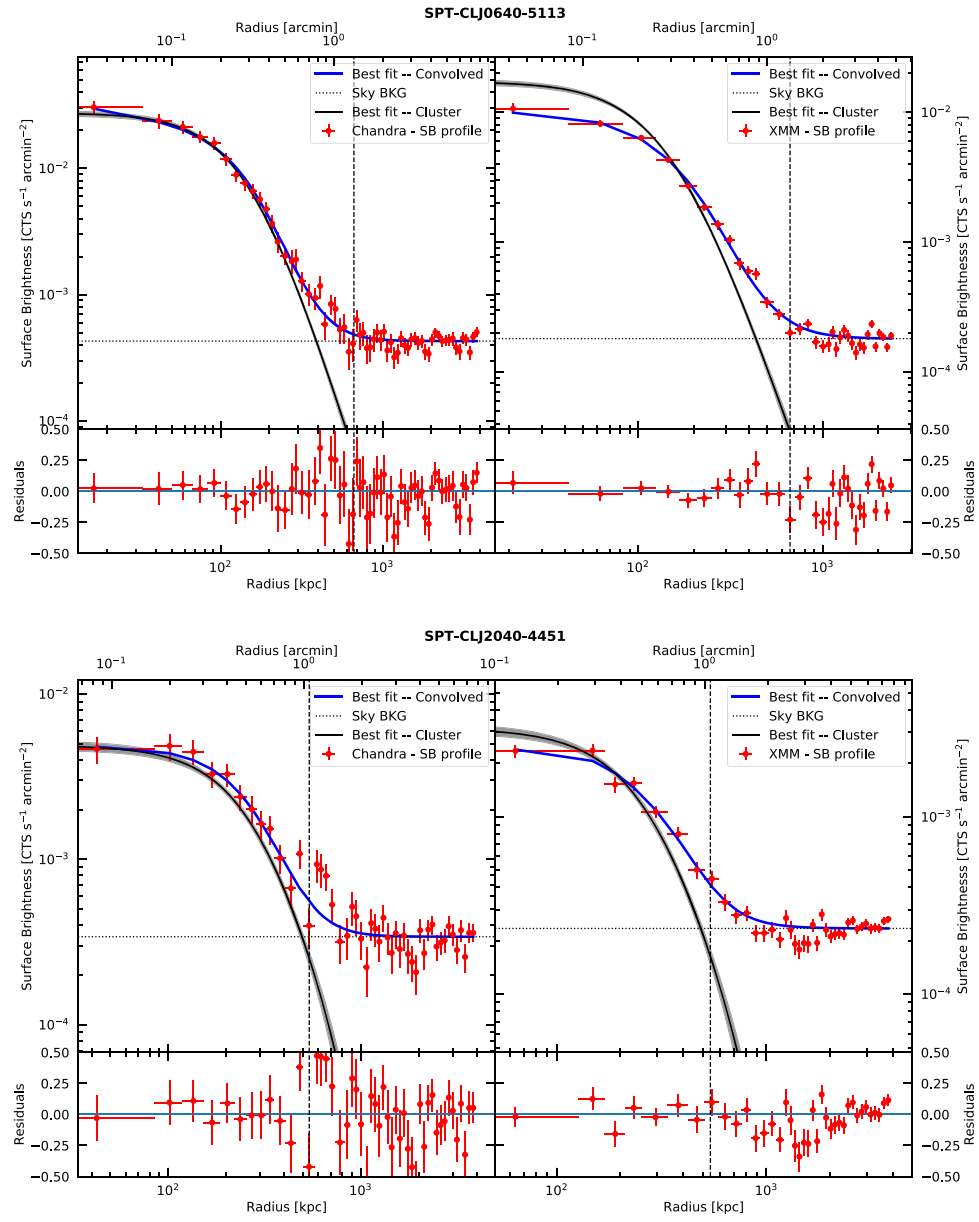


Figure A2. (Continued.)

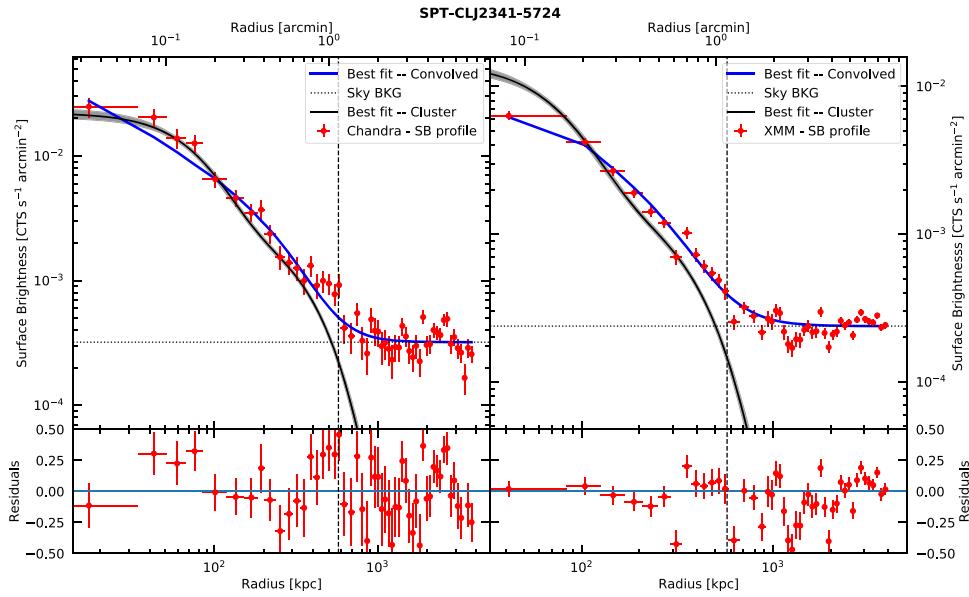


Figure A2. (Continued.)

Table 6

Information on the Cluster Recovered Temperatures within  $R_{500}$  (see Figure 11) and the Recovered Masses Using Different Techniques (see Appendix and Figure 10)

Cluster	$T_{\text{XMM}}$ (keV)	$T_{\text{CXO}}$ (keV)	$M_{\text{forward T}}$ ( $10^{14} M_{\odot}$ )	$M_{\text{forward P}}$ ( $10^{14} M_{\odot}$ )	$M_{\text{NFW, no c-M}}$ ( $10^{14} M_{\odot}$ )	$M_{\text{NFW, with c-M}}$ ( $10^{14} M_{\odot}$ )
SPT-CLJ0205-5829	$6.51^{+0.75}_{-0.57}$	$5.81^{+3.82}_{-0.82}$	$4.44 \pm 0.98$	$6.30 \pm 3.31$	$4.88 \pm 3.50$	$4.80 \pm 1.58$
SPT-CLJ0313-5334	$5.70^{+0.41}_{-0.67}$	$6.68^{+3.47}_{-2.61}$	$3.26 \pm 0.78$	$4.31 \pm 1.20$	$4.45 \pm 1.88$	$3.07 \pm 1.08$
SPT-CLJ0459-4947	$6.92^{+0.34}_{-0.33}$	$8.08^{+1.03}_{-1.61}$	$3.24 \pm 0.36$	$3.35 \pm 0.49$	$4.83 \pm 2.44$	$4.28 \pm 0.96$
SPT-CLJ0607-4448	$5.48^{+0.42}_{-0.48}$	$8.89^{+2.33}_{-2.21}$	$2.13 \pm 0.34$	$2.71 \pm 0.73$	$2.69 \pm 1.89$	$1.94 \pm 0.71$
SPT-CLJ0640-5113	$6.18^{+0.17}_{-0.52}$	$8.08^{+1.68}_{-1.39}$	$2.70 \pm 0.38$	$2.95 \pm 0.53$	$3.14 \pm 0.96$	$3.59 \pm 0.59$
SPT-CLJ2040-4451	$4.73^{+0.52}_{-0.48}$	$5.23^{+2.14}_{-1.44}$	$2.28 \pm 0.30$	$1.84 \pm 0.32$	$2.44 \pm 0.45$	$2.72 \pm 0.51$
SPT-CLJ2341-5724	$5.21^{+0.58}_{-0.40}$	$8.18^{+1.25}_{-2.60}$	$2.51 \pm 0.37$	$2.25 \pm 0.77$	$1.54 \pm 1.61$	$1.66 \pm 0.78$

## ORCID iDs

Vittorio Ghirardini <https://orcid.org/0000-0002-3736-8058>  
 Ralph Kraft <https://orcid.org/0000-0002-0765-0511>  
 Matt Bayliss <https://orcid.org/0000-0003-1074-4807>  
 Sebastian Bocquet <https://orcid.org/0000-0002-4900-805X>  
 Micheal Calzadilla <https://orcid.org/0000-0002-2238-2105>  
 Dominique Eckert <https://orcid.org/0000-0001-7917-3892>  
 William Forman <https://orcid.org/0000-0002-9478-1682>  
 Juan David Remolina Da González <https://orcid.org/0000-0002-7868-9827>  
 Gourav Khullar <https://orcid.org/0000-0002-3475-7648>  
 Guillaume Mahler <https://orcid.org/0000-0003-3266-2001>  
 Michael McDonald <https://orcid.org/0000-0001-5226-8349>

## References

Ameglio, S., Borgani, S., Pierpaoli, E., & Dolag, K. 2007, *MNRAS*, **382**, 397  
 Amodeo, S., Ettori, S., Capasso, R., & Sereno, M. 2016, *A&A*, **590**, A126  
 Andreon, S. 2012, *A&A*, **546**, A6  
 Arnaud, K. A. 1996, in ASP Conf. Ser. 101, *Astronomical Data Analysis Software and Systems V*, ed. G. H. Jacoby & J. Barnes (San Francisco, CA: ASP), 17  
 Arnaud, M., Pratt, G. W., Piffaretti, R., et al. 2010, *A&A*, **517**, A92  
 Ascasibar, Y., Sevilla, R., Yepes, G., Müller, V., & Gottlöber, S. 2006, *MNRAS*, **371**, 193  
 Asplund, M., Grevesse, N., Sauval, A. J., & Scott, P. 2009, *ARA&A*, **47**, 481  
 Avestruz, C., Nagai, D., & Lau, E. T. 2016, *ApJ*, **833**, 227  
 Bartalucci, I., Arnaud, M., Pratt, G. W., et al. 2017a, *A&A*, **598**, A61

Bartalucci, I., Arnaud, M., Pratt, G. W., et al. 2017b, *A&A*, **608**, A88  
 Bayliss, M. B., Ashby, M. L. N., Ruel, J., et al. 2014, *ApJ*, **794**, 12  
 Birzan, L., Rafferty, D. A., Brüggen, M., & Intema, H. T. 2017, *MNRAS*, **471**, 1766  
 Bleem, L. E., Stalder, B., de Haan, T., et al. 2015, *ApJS*, **216**, 27  
 Bocquet, S., Dietrich, J. P., Schrabback, T., et al. 2019, *ApJ*, **878**, 55  
 Bonamente, M., Hasler, N., Bulbul, E., et al. 2012, *NJPh*, **14**, 025010  
 Brodwin, M., McDonald, M., Gonzalez, A. H., et al. 2016, *ApJ*, **817**, 122  
 Bulbul, E., Chiu, I. N., Mohr, J. J., et al. 2019, *ApJ*, **871**, 50  
 Bulbul, E., Randall, S. W., Bayliss, M., et al. 2016, *ApJ*, **818**, 131  
 Bulbul, G. E., Hasler, N., Bonamente, M., & Joy, M. 2010, *ApJ*, **720**, 1038  
 Bulbul, G. E., Smith, R. K., Foster, A., et al. 2012, *ApJ*, **747**, 32  
 Capelo, P. R., Coppi, P. S., & Natarajan, P. 2012, *MNRAS*, **422**, 686  
 Carlstrom, J. E., Ade, P. A. R., Aird, K. A., et al. 2011, *PASP*, **123**, 568  
 Cash, W. 1979, *ApJ*, **228**, 939  
 Cavagnolo, K. W., Donahue, M., Voit, G. M., & Sun, M. 2009, *ApJS*, **182**, 12  
 Croston, J. H., Arnaud, M., Pointecouteau, E., & Pratt, G. W. 2006, *A&A*, **459**, 1007  
 De Grandi, S., & Molendi, S. 2002, *ApJ*, **567**, 163  
 Diehl, S., & Statler, T. S. 2006, *MNRAS*, **368**, 497  
 Diemer, B. 2017, arXiv:1712.04512  
 Diemer, B., & Joyce, M. 2018, arXiv:1809.07326  
 Eckert, D., Ettori, S., Coupon, J., et al. 2016, *A&A*, **592**, A12  
 Eckert, D., Ettori, S., Molendi, S., Vazza, F., & Paltani, S. 2013a, *A&A*, **551**, A23  
 Eckert, D., Ettori, S., Pointecouteau, E., et al. 2017, *AN*, **338**, 293  
 Eckert, D., Finoguenov, A., Ghirardini, V., et al. 2020, *OJAp*, **3**, 12  
 Eckert, D., Molendi, S., & Paltani, S. 2011, *A&A*, **526**, A79  
 Eckert, D., Molendi, S., Vazza, F., Ettori, S., & Paltani, S. 2013b, *A&A*, **551**, A22  
 Eckert, D., Roncarelli, M., Ettori, S., et al. 2015, *MNRAS*, **447**, 2198  
 Ettori, S., Donnarumma, A., Pointecouteau, E., et al. 2013, *SSRv*, **177**, 119

- Ettori, S., Gastaldello, F., Leccardi, A., et al. 2010, *A&A*, **524**, A68
- Ettori, S., Ghirardini, V., Eckert, D., et al. 2018, arXiv:1805.00035
- Ettori, S., & Molendi, S. 2011, *MSAIS*, **17**, 47
- Fabian, A. C., Sanders, J. S., Crawford, C. S., & Ettori, S. 2003, *MNRAS*, **341**, 729
- Fakhouri, O., & Ma, C.-P. 2009, *MNRAS*, **394**, 1825
- Fakhouri, O., Ma, C.-P., & Boylan-Kolchin, M. 2010, *MNRAS*, **406**, 2267
- Feroz, F., Hobson, M. P., & Bridges, M. 2009, *MNRAS*, **398**, 1601
- Foreman-Mackey, D., Hogg, D. W., Lang, D., & Goodman, J. 2013, *PASP*, **125**, 306
- Foster, A. R., Ji, L., Smith, R. K., & Brickhouse, N. S. 2012, *ApJ*, **756**, 128
- Fowler, J. W., Niemack, M. D., Dicker, S. R., et al. 2007, *ApOpt*, **46**, 3444
- Fruscione, A., McDowell, J. C., Allen, G. E., et al. 2006, *Proc. SPIE*, **6270**, 62701V
- Gao, F., & Han, L. 2012, *Comput. Optim. Appl.*, **51**, 259
- Gaskin, J. A., Swartz, D. A., Vikhlinin, A., et al. 2019, *JATIS*, **5**, 021001
- Ghirardini, V., Eckert, D., Ettori, S., et al. 2018a, arXiv:1805.00042
- Ghirardini, V., Ettori, S., Eckert, D., et al. 2018b, *A&A*, **614**, A7
- Ghirardini, V., Ettori, S., Eckert, D., & Molendi, S. 2019, *A&A*, **627**, A19
- Gonzalez, A. H., Sivanandam, S., Zabludoff, A. I., & Zaritsky, D. 2013, *ApJ*, **778**, 14
- Goodman, J., & Weare, J. 2010, *CAMCS*, **5**, 65
- Grant, C. E., Bautz, M. W., Kissel, S. M., LaMarr, B., & Prigozhin, G. Y. 2005, *Proc. SPIE*, **5898**, 201
- Hasler, N., Bulbul, E., Bonamente, M., et al. 2012, *ApJ*, **748**, 113
- Hlavacek-Larrondo, J., Fabian, A. C., Edge, A. C., et al. 2012, *MNRAS*, **421**, 1360
- Kaiser, N. 1986, *MNRAS*, **222**, 323
- Kalberla, P. M. W., Burton, W. B., Hartmann, D., et al. 2005, *A&A*, **440**, 775
- Khedekar, S., Churazov, E., Kravtsov, A., et al. 2013, *MNRAS*, **431**, 954
- Khullar, G., Bleem, L. E., Bayliss, M. B., et al. 2019, *ApJ*, **870**, 7
- Komatsu, E., & Seljak, U. 2001, *MNRAS*, **327**, 1353
- Kravtsov, A. V., & Borgani, S. 2012, *ARA&A*, **50**, 353
- Leccardi, A., & Molendi, S. 2008, *A&A*, **486**, 359
- Markevitch, M., Forman, W. R., Sarazin, C. L., & Vikhlinin, A. 1998, *ApJ*, **503**, 77
- Mazzotta, P., Rasia, E., Moscardini, L., & Tormen, G. 2004, *MNRAS*, **354**, 10
- McDonald, M., Allen, S. W., Bayliss, M., et al. 2017, *ApJ*, **843**, 28
- McDonald, M., Benson, B. A., Vikhlinin, A., et al. 2013, *ApJ*, **774**, 23
- McDonald, M., Benson, B. A., Vikhlinin, A., et al. 2014, *ApJ*, **794**, 67
- McDonald, M., Stalder, B., Bayliss, M., et al. 2016, *ApJ*, **817**, 86
- Nagai, D., Kravtsov, A. V., & Vikhlinin, A. 2007, *ApJ*, **668**, 1
- Nandra, K., Barret, D., Barcons, X., et al. 2013, arXiv:1306.2307
- Navarro, J. F., Frenk, C. S., & White, S. D. M. 1997, *ApJ*, **490**, 493
- Neto, A. F., Gao, L., Bett, P., et al. 2007, *MNRAS*, **381**, 1450
- Ostriker, J. P., Bode, P., & Babul, A. 2005, *ApJ*, **634**, 964
- Planck Collaboration, Ade, P. A. R., Aghanim, N., et al. 2014, *A&A*, **571**, A20
- Planck Collaboration, Ade, P. A. R., Aghanim, N., et al. 2016, *A&A*, **594**, A13
- Pratt, G. W., Arnaud, M., Piffaretti, R., et al. 2010, *A&A*, **511**, A85
- Pratt, G. W., Croston, J. H., Arnaud, M., & Böhringer, H. 2009, *A&A*, **498**, 361
- Read, A. M., Rosen, S. R., Saxton, R. D., & Ramirez, J. 2011, *A&A*, **534**, A34
- Roncarelli, M., Ettori, S., Borgani, S., et al. 2013, *MNRAS*, **432**, 3030
- Rossetti, M., Gastaldello, F., Eckert, D., et al. 2017, *MNRAS*, **468**, 1917
- Salvetti, D., Marelli, M., Gastaldello, F., et al. 2017, arXiv:1705.04172
- Sanders, J. S., Fabian, A. C., Russell, H. R., & Walker, S. A. 2018, *MNRAS*, **474**, 1065
- Sanderson, A. J. R., Ponman, T. J., Finoguenov, A., Lloyd-Davies, E. J., & Markevitch, M. 2003, *MNRAS*, **340**, 989
- Schellenberger, G., Reiprich, T. H., Lovisari, L., Nevalainen, J., & David, L. 2015, *A&A*, **575**, A30
- Shaw, L. D., Nagai, D., Bhattacharya, S., & Lau, E. T. 2010, *ApJ*, **725**, 1452
- Shitanishi, J. A., Pierpaoli, E., Sayers, J., et al. 2018, *MNRAS*, **481**, 749
- Snowden, S. L., Mushotzky, R. F., Kuntz, K. D., & Davis, D. S. 2008, *A&A*, **478**, 615
- Stalder, B., Ruel, J., Šuhada, R., et al. 2013, *ApJ*, **763**, 93
- Tillson, H., Miller, L., & Devriendt, J. 2011, *MNRAS*, **417**, 666
- Tozzi, P., Santos, J. S., Jee, M. J., et al. 2015, *ApJ*, **799**, 93
- Urban, O., Simionescu, A., Werner, N., et al. 2014, *MNRAS*, **437**, 3939
- Urban, O., Werner, N., Simionescu, A., Allen, S. W., & Böhringer, H. 2011, *MNRAS*, **414**, 2101
- Vikhlinin, A., Kravtsov, A., Forman, W., et al. 2006, *ApJ*, **640**, 691
- Vikhlinin, A., Kravtsov, A. V., Burenin, R. A., et al. 2009, *ApJ*, **692**, 1060
- Voit, G. M., Kay, S. T., & Bryan, G. L. 2005, *MNRAS*, **364**, 909
- Walker, S., Simionescu, A., Nagai, D., et al. 2019, *SSRv*, **215**, 7
- Walker, S. A., Fabian, A. C., Sanders, J. S., & George, M. R. 2012, *MNRAS*, **424**, 1826
- Wechsler, R. H., Bullock, J. S., Primack, J. R., Kravtsov, A. V., & Dekel, A. 2002, *ApJ*, **568**, 52
- Zhuravleva, I., Churazov, E., Kravtsov, A., et al. 2013, *MNRAS*, **428**, 3274